UNIVERSITÉ DE
SHERBROOKE

Faculté de génie

Département de mécanique

MICROUSINAGE DE VERRE PHOTOSENSIBLE PAR EXPOSITION UV AVEC UN LASER EXCIMÈRE ArF ($193nm$)

Mémoire de maîtrise en génie

Spécialité : Génie mécanique

Membres du jury:

Patrice Masson

Jan Dubowski

Luc Fréchette

Joël DION

Sherbrooke (Québec), CANADA Décembre 2008

SUMMARY

Glass is a technologically important material finding numerous applications in photonics and optoelectronics. In the recent decade, we have also observed a growing interest in exploring the potential of this material for the manufacture of micro-electro-mechanical systems (MEMS). Conventional methods for micromachining of glass are prohibitively slow, and laser ablation leads to macrocracks and rough surfaces morphologies. In that context, photosensitive glass ceramics, such as Foturan^{TM}, offer significant advantages in fabrication of commercial grade, optically transparent, two- and three-dimensional (2D and 3D) microstructures. To address the problem of rapid fabrication of such microstructures with smooth surface morphology, we have undertaken a study of micromachining of Foturan^{TM} with an ArF excimer laser ($\lambda = 193nm$) mask projection system. To our knowledge, this is the shortest wavelength laser ever used for processing of Foturan^{TM}.

The applied micromachining technique consists of three major steps: 1) Irradiation with the laser, 2) High-temperature annealing and, 3) Wet etching to remove the irradiated and annealed glass volume. Due to the strong optical absorption at 193 nm, it was expected that a better control could be achieved of the machined surface morphology when compared to the previously reported results obtained with 266 and 355 nm lasers, or with femtosecond lasers. At the same time, the application of the excimer laser mask projection should allow processing of relatively large dimension wafers.

We have demonstrated that a one-step irradiation approach allows fabricating craters with the maximum depth not exceeding 35 μm. Deeper craters, up to 120 μm, have been fabricated following a series of irradiation-annealing-etching steps. We have fabricated a series of complex $3D$ microstructures using special masks and a mask scanning technique. The amplitude of the surface roughness of as-fabricated microstructures was, typically, not worse than 100 nm. This is expected to be reduced to less than 10 nm by implementing post-processing annealing. The results of this study have indicated clearly the feasibility of the 193 nm excimer laser and the mask projection technique for rapid fabrication of $3D$ microstructures in photosensitive glass. The proposed method is expected to find applications in the fabrication of, e.g., shallow microfluidic devices, or a specialty of optoelectronic devices.

RÉSUMÉ

Le verre est un matériau prometteur qu'on retrouve dans de nombreuses applications en photonique et en optoélectronique. Au cours de la dernière décennie, un intérêt croissant a été porté sur ce matériau pour la fabrication de micro système électro-mécanique. Les méthodes conventionnelles de micro-usinage de verre sont trop lents, et l'ablation laser conduit à des fissures et une rugosité élevée. Dans ce contexte, le verre photosensible, tels que le Foturan^{TM}, offrent des avantages notables dans la fabrication de microstructures à deux ou trois dimensions. Pour aborder le problème de fabrication rapide de ces microstructures à faible rugosité, nous avons entrepris une étude de micro-usinage de Foturan^{TM} avec un laser excimère ARF ($\lambda = 193nm$). À notre connaissance, c'est la plus courte longueur d'onde laser jamais utilisée pour l'irradiation du Foturan^{TM}.

Cette technique de micro-usinage se compose de trois grandes étapes: 1) Irradiation laser, 2) traitement thermique et, 3) gravure humide pour éliminer le volume de zones irradiés et recuit. En raison de la forte absorption optique à 193 nm, on s'attendait à ce qu'un meilleur contrôle pourrait être réalisé de l'usinage de la surface par rapport aux résultats précédemment obtenus avec des lasers excimère à 266 et 355 nm, ou avec des lasers femtoseconde. De plus, l'utilisation d'une technique de projection de masques permet l'irradiation de gaufres de dimension relativement importante.

Nous avons démontré que la technique permet la fabrication de cratères avec une profondeur maximale ne dépassant pas 35 μm. Des cratères plus profond, jusqu'à 120 μm, ont été fabriqués à la suite d'une série d'irradiation-recuit-gravure. Nous avons fabriqué une série de structures complexes en $3D$ en utilisant la technique de projection de masques et le balayage du laser. La rugosité de surface des microstructures qui ont été fabriqués sont de l'ordre de 100 nm. Ce qui pourrait être réduits à moins de $10nm$ par la mise en oeuvre d'un post-traitement de recuit. Les résultats de cette étude ont indiqué clairement la faisabilité de l'utilisation du laser excimère à 193 nm combiné à la projection de masques pour la fabrication rapide de microstructures en verre photosensible en $3D$. Le méthode proposée devrait trouver des applications dans le domaine de la fabrication, par exemple, des dispositifs microfluidiques, ou des composantes spécialisés d'optoélectroniques.

Mots-clés: Foturan, laser excimère ArF, photosensible, gravure HF.

TABLE OF CONTENTS

LIST OF TABLES

LIST OF FIGURES

CHAPTER 1

INTRODUCTION

1.1 Development of micro-electro mechanical systems

The miniaturization of mechanical and/or electrical devices has been the result of continuous advancements of microfabrication technologies. In this context, a new class of products appeared under the name of MEMS "**M**icro-**E**lectro **M**echanical **S**ystem". One of the first industrial devices to be commercialised in 1993 by *Analog Devices* is an accelerometer which made possible a reduction in the installation cost of airbag systems [Wisniowski, 1999]. Following these first devices with mechanical and electrical functions, a new generation of devices now emerges on the market, with photonic and fluidic systems. These devices, called lab-on-a-chip or μ-Tas (micro total analysis system), accelerate chemical reactions and consequently allow for faster analysis [Masuda, M. *et al.*, 2003, Sugioka, K. *et al.*, 2005]. One example of such lab-on-a-chip devices was developed by *Nanogen* [Dario, P. *et al.*, 2000]. This chip contains both cells where the molecular analysis takes place and reserved tanks that enable the reaction. The two most important advantages of this device are: firstly, the possibility to fabricate the devices in batch production and secondly, the small quantity of sampling materials necessary for the analysis [Karnakis, D.M. *et al.*, 2005]. Moreover, these advantages lead to a reduction of the actual costs.

Lab-on-a-chip devices results from miniaturization and automation of laboratory process for chemical analysis and they are widely fabricated using glass substrates [Khan Malek *et al.*, 2006]. These devices have many advantages, but the most important one is the possibility of accomplishing biochemical analysis rapidly on a small footprint [Fruman, D.H., 2001, Cheng *et al.*, 2005]. An example of such systems is a device for DNA analysis described by J-E Kim [Kim *et al.*, 2005]. This device, like other ones of this generation, was fabricated with conventional techniques from microelectronics. The latter are based

on photolithography and are consequently limited to the design of $2D$ devices.

1.2 Problem to be addressed

Novel technological advancements are required to allow fabrication of $2.5D$ ($2D$ with discrete multiple levels) or real $3D$ microstructures. For instance, laser ablation has been investigated for the fabrication of $3D$ microstructures. Unfortunately, direct ablation of materials suffers from limited control of the surface morphology, which results in limited control of the process spatial resolution.

We are interested in exploring a laser-based technology to develop a 3D microstructuring process capable of delivering high-quality surface using an etching procedure. Such a process could be based on laser exposure of photosensitive glass followed by selective etching.

1.3 Organization of the thesis

This document presents the result of experiments focussed on the realization of such a machining method using an ultraviolet radiation (UV) from an ArF excimer laser.

In chapter 2, a literature review is presented. This chapter permits to explain the context and the utility of the new process. The first part of this chapter concerns the microscale applications of glass. Next, machining methods for glass are presented. Three conventional methods are presented: chemical etching used by micro-electronics industry, laser ablation and a method which combines a water jet system and a laser. Finally, the chapter ends with a short review of the previous work on the studied process.

The third chapter presents the problem addressed in this work and the objectives of the project. The fourth chapter presents the experimental setup. Four different experimental equipments are described. Firstly, two laser stations with an ArF excimers are described (GAUS laser station and QS Group laser station), secondly, are described the furnace for the annealing process and the characterization tools.

Chapter five presents the experimental process and the results. It is divided into three sections: 1). Preliminary experiments that served to establish the machining conditions; 2). Discussion of the process parameters. In this section, each parameter is studied and its influence on the process is shown; 3). Presentation of a new approach to improve the versatility of this machining process.

The last chapter discusses the results of the previous chapter. Moreover, it shows examples of more complex structures and some indications to help resolve future problems which can appear with the machining process.

CHAPTER 2

LITERATURE REVIEW

2.1 Microscale applications of glass

The use of glass in the field of MEMS has many advantages [Cheng *et al.*, 2005]. One of these is the transmittance in the visible electromagnetic spectrum. Another advantage is its chemical stability [Khan Malek *et al.*, 2006, Rajta, I. *et al.*, 2003]. These unique properties allow the integration of photonic devices with fluidic systems. For instance, Cheng [Cheng *et al.*, 2005] designed and fabricated a microfluidic structure with a free-standing optical fiber incorporated on the same substrate. Moreover, due to its attractive mechanical properties (stiffness, toughness, and high temperature resistance), glass is a material of choice to realize multi-functional structures like small spacecraft [Janson, S.W. and Helvajian, H., 1999]. This section discusses a number of microscale applications of glass.

2.1.1 Photonic devices

Photonics refers to the science and technology for generating, controlling, and detecting photons, particularly in the visible light and near infra-red spectrum [Wikipedia, 2008]. This section discusses phototonic technologies.

For complex photonic devices, many substrates are conceivable, including silicon, photosensitive resins and glass. Silicon has many advantages, but its transparency is limited to $1.5\mu m$ [Almaz Optics, 2006], and it is opaque in the visible spectrum. For photosensitive resins, the problem is not the transmittance in the visible spectrum, but their mechanical stiffness.

The third material is glass which is already used largely in the fabrication of optical fibers. Despite extensive research on optical fibers, most of the work has been limited to one dimensional devices, optical fiber. One of the advantages of glass in comparison to the photosensitive resins is its mechanical stiffness. For example, the SU-8 resin has a Young's modulus of $4.02GPa$ [Feng and Farris, 2002] and glass has about $80GPa$ [Feng and Farris, 2002]. Furthermore, glass is more transparent in UV than SU-8 resin.

Many experiments were conducted on the use of Foturan glass for photonic devices. For instance, Cheng has realized freestanding optical fibers in glass substrate [Cheng *et al.*, 2005]. The technique he used is based on femtosecond irradiation followed by an annealing process. A complete description of these two steps is presented in chapter 4. He used a femtosecond laser at 775nm with a pulse rate of 1KHz and a pulse length of 145fs. The refractive index modification is the result of precipitation of silver nanoparticles [Cheng *et al.*, 2005]. Unfortunately, this modification comes with an increase of optical loss which was measured by Cheng to be 0.7dB/cm.

A year later, Cheng published some results about a new photonic device [Cheng *et al.*, 2006]. He realized a 3D microoptical lens in photosensitive glass. This time, the photonic device is not only a modification of the refractive index but a modification of the shape of the glass. For this, a third step is necessary, i.e. etching. This step will be detailed in section 2.2.4.

Cheng [Cheng *et al.*, 2006] used a femtosecond laser at 800nm, with a pulse rate of 1kHz and pulse length of 120fs. Figure 2.1 a) shows the result after the etching step. To obtain a better surface smoothness, a second annealing at $560°C$ for 5 hours is realized. The mechanism for this annealing step is comparable to the surface of melting ice. A thin layer of liquid glass appears at the surface and allows for a smoother surface after the decreased temperature. The result is shown in Figure 2.1 b). This lens focuses a He-Ne laser ($632nm$) with a beam waist of $0.7mm$ to a focal spot of about $30 \sim 40\mu m$ [Cheng *et al.*, 2006].

A second method was studied by Bhardwaj, to realize waveguides on Foturan by direct writing with femtosecond laser [Bhardwaj *et al.*, 2005]. The femtosecond laser is directly focused in the substrate and a positive refractive index change was observed at the focal point. From his observation, he concluded that the refractive index change is the result of ion migration. Another research group has studied the same approach to

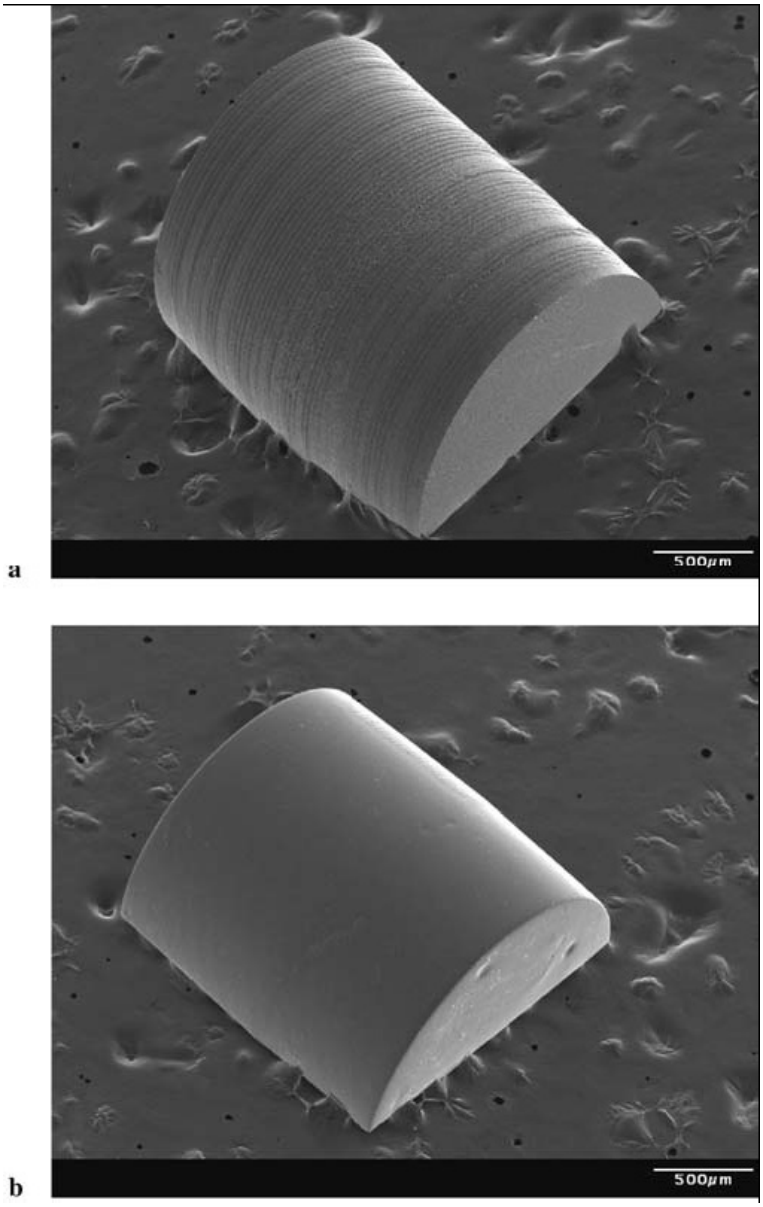

Figure 2.1 SEM images of micro cylinder lenses realized by Cheng [Cheng *et al.*, 2006] a) Without smoothening stage b) With smoothening stage

realize waveguides. They measured a transmission loss [An *et al.*, 2007] similar to the one measured by Cheng [Cheng *et al.*, 2005]. The transmission loss measured with a He-Ne laser at ($632nm$) was about 0.8dB/cm. This second approach is interesting because it requires only one step to realize waveguides.

Another approach to direct writing of waveguides in photosensitive glass is demonstrated by Bettiol [Bettiol *et al.*, 2006]. He used a proton beam to expose the glass. The modification of the refractive index is comparable to one obtained by femtosecond irradiation, i.e. 1.6×10^{-3}.

2.2 Machining methods of glass

This section presents an overview of some methods for the machining of glass. The focus is on the machining of Foturan glass. However, as the mechanical properties of Foturan are similar to other glasses, the same machining methods can be used and they are therefore presented here.

2.2.1 Conventional methods from microelectronics

Most microelectronic devices are fabricated from silicon wafers. The electronics structures are built on the surface by deposition of material, growing and etching. To create layers with desired patterns, masks and photolithography process are used.

In the case of glass, the standard steps to machining are photolithography and etching processes. The etching of glass is achieved by:

- Wet chemical etching;
- Vapor etching;
- Plasma-assisted etching;
- Deep reactive ion etching (DRIE).

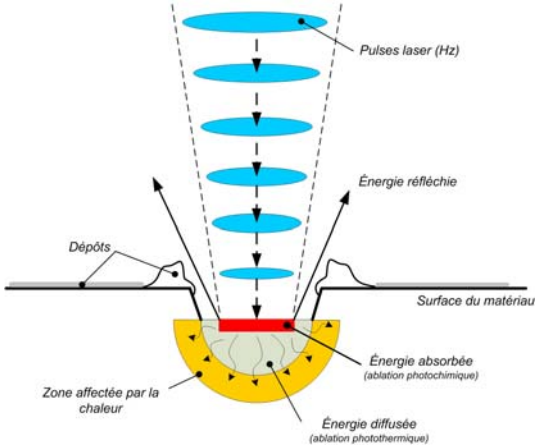

Figure 2.2 Photochemical and photothermal ablation [Desbiens, 2006]

Except for the last process, the major disadvantage of these methods is their low anisotropy. In fact, (DRIE) has shown that anisotropy to the order of 1 : 100 is feasible [Frechette *et al.*, 2000]. Moreover, all these methods are photolithography-based processes, which make them perfectly adapted to high volume production although they are expensive for low volume device prototyping.

2.2.2 Laser photoablation

Laser ablation machining results from the combination of two processes: photochemical and photothermal ablation. Figure 2.2, adapted from J.-P. Desbiens [Desbiens, 2006], illustrates the interaction between laser beam and material. The photochemical ablation results in the destruction of atomic bonds after photonic absorption. In the photothermal process, an increase in the temperature melts and vaporizes the material [Desbiens, 2006]. The photothermal process represents one of the drawbacks of this method since the high temperature gradient might deteriorate the material by creating cracks [Karnakis, D.M. *et al.*, 2005]. The relative contribution of chemical and thermal ablation processes depends on the material and the laser properties.

Five laser types are principally used for micromachining:

- CO_2 laser ($\lambda = 10.6\mu m$)
- Nd:YAG laser ($\lambda = [266, 355, 532, 1060, 1320]nm$)

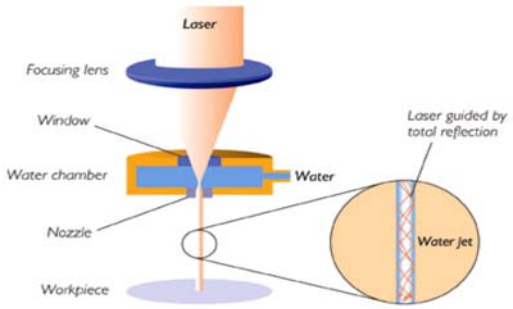

Figure 2.3 *Waterjet* system [Sibailly and Richerzhagen, 2004]

- CVL laser (Copper Vapour Laser) ($\lambda = [511, 578]\mu m$)
- excimer nanosecond and femtosecond laser ($\lambda = [157, 193, 222, 248, 282, 308, 351]nm$)
- other femtosecond lasers ($\lambda = [780, 800]nm$)

2.2.3 Laser machining combined with water jet system

This method combines two proven machining techniques. The first one is laser photoablation and the second one, water jet cutting. The goal of this combination is to reduce the temperature near the cut and consequently to reduce thermal stress [Sibailly and Richerzhagen, 2004]. Additionally, the use of the water jet allows a faster evacuation of debris. The advantage of this method in comparison to machining with conventional laser beams is the possibility of limiting laser beam divergence. This is due to the fact that the water jet acts as a waveguide and allows for the transmission of a highly concentrated laser beam. Another advantage is that this combination required water jet pressure at 50 to $500 bars$, which compares to $3000 bars$ required by traditional water jet cutting techniques. Thus, this machining method offers two main advantages: firstly, the low temperature gradient from the water jet and secondly, the low mechanical stress from laser machining.

Today, laser machining combined with water jet system is principally used for die cutting. Figure 2.3, from Sibailly [Sibailly and Richerzhagen, 2004], shows the process. We can see on it the waveguide formed by the water jet.

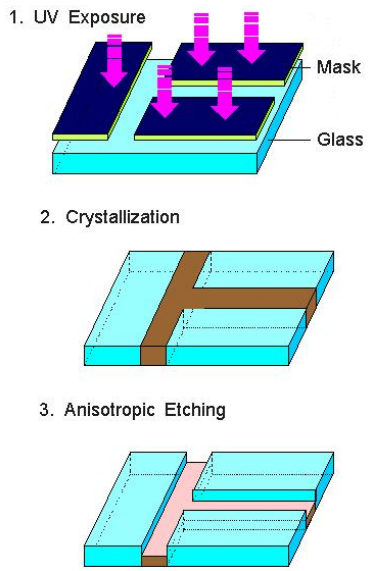

Figure 2.4 Steps involved in the machining of photoetchable glass [Dietrich, T.R. *et al.*, 1996]

2.2.4 Machining by photo exposure

This method requires a photosensitive material. The photosensitivity of the material results from certain atoms in the glass, like cerium and silver [Dietrich, T.R. *et al.*, 1996]. Only a small number of types of glass have this propriety; consequently, the method has not been sufficiently popularized yet. The most known photosensitive glass is *Foturan*. It contains cerium in the form of Ce_2O_3 molecules and its concentration is about 0.01% to 0.04% [Dietrich, T.R. *et al.*, 1996].

The machining technique of Foturan consists of photo-exposure to modify the properties of the glass. This modification makes glass more reactive to subsequent wet etching. This machining method consists of four steps. Figure 2.4 shows three of these steps. The first one is the photo exposure.

Stage 1: Photo exposure

This stage defines the shape of the structure achieved after all the stages are completed [Dietrich, T.R. *et al.*, 1996]. Two pieces of equipment are most frequently used to realize photo exposure, the MeV protons [Gomez-Morilla, I. *et al.*, 2005,Rajta, I. *et al.*, 2003] and the laser. As the laser is principally used, this text will only discuss the latter system.

The glass is first exposed to a laser beam. The latter has to be sufficiently energetic to reach the dose threshold. The dose threshold is defined by the minimal dose in order to obtain the crystalline state which makes the glass soluble in hydrofluoric acid [Hongo *et al.*, 2005]. This lower energy threshold depends on the exposure wavelength [Juodkazis, S. *et al.*, 2004].

As a result of photo exposure, the increase in temperature allows the creation of Ce^{3+} ions [Kim *et al.*, 2004]. The chemical formula for this reaction is:

$$2Ce^{4+} + Sb^{3+} \longleftrightarrow 2Ce^{3+} + Sb^{5+} \tag{2.1}$$

Afterwards, the newly formed ions of Ce^{4+} absorb photons and return to their previous form (Ce^{3+}) by emitting electrons:

$$Ce^{3+} + photon \longrightarrow Ce^{4+} + e^{-} \tag{2.2}$$

Finally, the free electrons bind with silver ions (Ag^{+}) to form silver atoms:

$$Ag^{+} + e^{-} \longrightarrow Ag \tag{2.3}$$

The exact moment at which this last reaction takes place is still the object of many investigations. Some researchers claim that the reaction takes place during the photo exposure while others suggest that it takes place during the annealing process [Cheng, Y. *et al.*, 2003]. The latter is described in the following section.

Stage 2: Annealing process

The annealing process allows the crystallization of lithium metasilicate on silver agglomerates [Kim *et al.*, 2004]. This process determines the surface roughness of the final structure. Indeed, the surface roughness is directly proportional to the size of the glass crystals [Cheng, Y. *et al.*, 2005] which have the diameter of about $1\mu m$ to $10\mu m$.

The most commonly used annealing process, and the one used for this project, consists first of an increase in temperature up to $500°C$ at a rate of $5°C/min$. During this first part of the annealing process, silver atoms diffuse to form agglomerates [Kim *et al.*, 2004]

with a diameter of about $8nm$ [Sugioka, K. *et al.*, 2005]. If the process is stopped just after this first step, modifications done during the time period stay permanently in the glass. Indeed, the nano-particles increase the refraction index of the glass [Cheng *et al.*, 2005]. This property can be exploited in some photonic structures. An example of the use of this first step is the fabrication of Bragg gratings on optical fibers used in precise wavelength filtering [Kösters, M. *et al.*, 2005]. These gratings are however not made in Foturan but in other types of glasses. Unfortunately, the increase in the refraction index also causes an increase in the absorption coefficient [Ho, S. and Herman, R., 2004, Cheng *et al.*, 2005].

The glass is kept at this temperature for one hour before it is reheated to $605°C$ at a rate of $3°C/minute$. This higher temperature favours the crystallization process around the sites created by silver agglomerates [Kim *et al.*, 2004]. The glass is kept at this temperature for another hour and finally, it is left to cool down to ambient temperature.

Stage 3: Etching

The etching is the third essential stage to conduct Foturan machining. Indeed, hydrofluoric acid solution preferably dissolves the exposed glass compared to the non-exposed glass [Kim *et al.*, 2004, Fuqua, P.D. *et al.*, 2000]. Consequently, after the etching step, the non-exposed Foturan reveals the structure. Further, to obtain a surface roughness better than $10\mu m$ an additional step is needed: the surface smoothening annealing.

The wet etching is accomplished with hydrofluoric acid (HF). Some experiments were conducted with concentrations of 5% to 40%. Schott, the manufacturer of Foturan, recommends a concentration of 10% and we will follow these recommendations. The HF concentration influences the maximum etching rate, but not the selective etching of the exposed glass area with respect to non-exposed glass area. A definite value for selectivity is not available in literature: some researchers obtained values around 20:1 while others obtained values around 50:1 [Cheng *et al.*, 2005, Kim *et al.*, 2004]. This selective etching is a function of irradiation power [Livingston, F.E. *et al.*, 2004] and it reaches a maximum value of about three times the threshold [Juodkazis, S. *et al.*, 2004]. The chemical formula for the etching of crystal glass is:

$$Li_2SiO_3 + 8HF \longrightarrow 2LiF + H_2SiF_6 + 3H_2O \tag{2.4}$$

The maximum etching rate measured is about $20\mu m/min$ [Livingston, F.E. and Helvajian, H., 2005]. Finally, it is important to note that the maximum etching rate is independent of the wavelength [Livingston, F.E. and Helvajian, H., 2005, Livingston, F.E. *et al.*, 2004].

Stage 4: Surface smoothening annealing

This last stage is used to reduce the surface roughness [Fuqua, P.D. *et al.*, 2000]. This is necessary if a Foturan-based device is to be used for photonic applications [Cheng, Y. *et al.*, 2005]. Indeed, light losses are in direct relation with the surface roughness: the higher the surface roughness, the higher the light losses.

This annealing process needs an increase in temperature to $560°C$ kept for 5h. With this process, it is possible to obtain a surface roughness of $0.8nm$ [Cheng, Y. *et al.*, 2005]. During this step, a thin layer of liquid glass is formed [Cheng *et al.*, 2006]. The surface tension of the liquid contributes to form a smoother surface. The temperature has to be precisely adjusted. If the thickness of the layer is too high, the surface tension is not adequate to overcome the gravity force. On the other hand, if the layer is too thin, the roughness is not swamped by the liquid.

Experimental results

Since this research focuses on the first of three stages of processing, only the results for photosensitivity will be presented. Until now, infrared and ultraviolet lasers are used for machining by photosensitivity. The two categories has advantages over the other. This section present experimental results obtained with both types of laser.

Sugioka has investigated the machining by photosensitization with a femtosecond IR laser [Sugioka, K. *et al.*, 2005]. He used a laser with wavelength of $775nm$ and a pulse duration of $140fs$. He measured the critical fluence that allows selective etching for different laser pulses. Figure 2.5 shows the results. He then estimated the equation that defines the critical dose. This equation is:

$$D_c = 1.35 * 10^{-5} J^6/cm^{12} \tag{2.5}$$

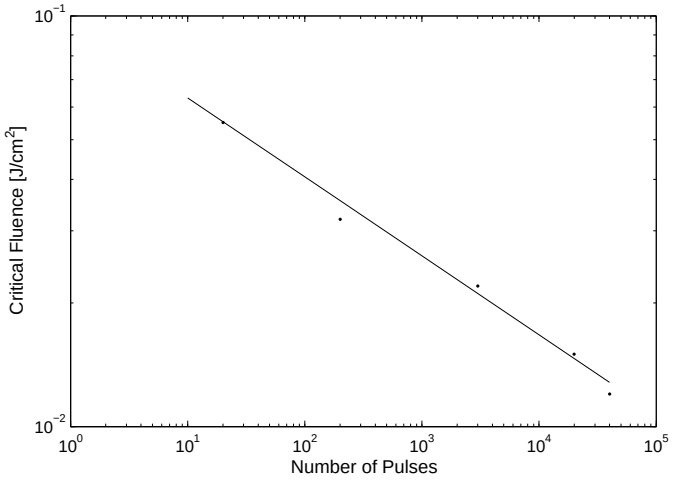

Figure 2.5 Dependence of critical fluence on the number of laser pulses [Sugioka, K. *et al.*, 2005]

Fisette has made similar experience with a laser at $800nm$ [Fisette and Meunier, 2004]. He estimated a different equation for the critical dose from that of Sugioka:

$$D_c = 1.36 * 10^4 J^7/cm^{14} \tag{2.6}$$

The main difference between the two equations is the power dependence. Another power dependance than one is caused by the energy of a photon at this wavelength it is insufficient to trigger the reaction. Thus, there is a multi-photons process (6 or 7). This provides the opportunity to machine under the surface without damaging the upper layers.

Inversely, UV lasers are absorbed by the Foturan. Livingston has measured an absorption coefficient of $10.05/cm$ with a wavelength of $266nm$ and $0.27/cm$ for $355nm$ [Livingston, F.E. *et al.*, 2004]. It is noted that decreasing the wavelength increases the absorption coefficient. Figure 2.6 shows the depth of crystallization according to the fluence for one laser pulse. It is consequently possible to fabricated surface structures at multiple levels by varying the laser fluence.

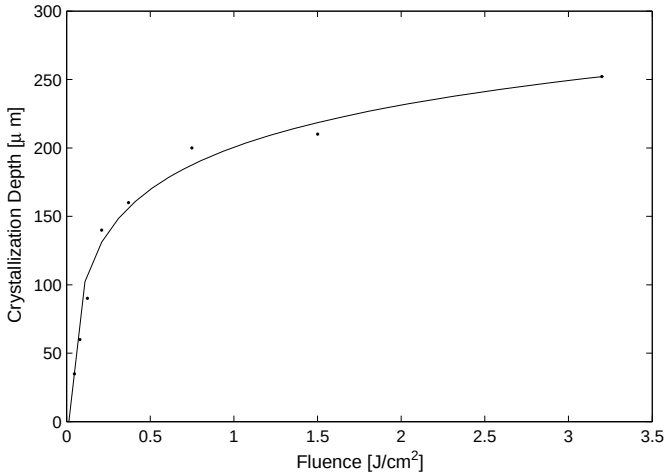

Figure 2.6 Dependence of the crystallization depth on the fluence [Kim *et al.*, 2004]

2.3 Devices based on Foturan glass

One of the first publications on the subject was written by Janson [Janson, S.W. and Helvajian, H., 1999]. They fabricated a micro converging/diverging nozzle in Foturan (Figure 2.7). The advantage of this device compared to others fabricated in silicon is that the mechanical robustness of Foturan that is harder than silicon [Janson, S.W. and Helvajian, H., 1999]. Moreover, this glass has a higher melting point than classical glass [Livingston, F.E. and Helvajian, H., 2005]. In silicon, the fabrication of micronozzles is realized by selective chemical etching using a solution of KOH, which induces a limitation on the geometry that can be fabricated. For instance, the cavities etched with KOH on silicon have a pyramidal shape. Another example of a Foturan-based device are micro-propellers by Larangot [Larangot, B. *et al.*,]. The low thermal conductivity allows for a decrease in the thickness of the wall between two adjacent micro-propellers without risk of a chain reaction to light up a nano-satellite equipped with such micro-propellers.

The first equation describing the photo exposition machining principle was published by Fuqua [Fuqua, P.D. *et al.*, 2000]. Since the release of these first equation, many other complex structures were built by the research group. Among them, one can mention a "Y" shape mixer. Its channels are $17\mu m$ by $71\mu m$ and are located $200\mu m$ under the surface [Masuda, M. *et al.*, 2003].

The same group has reported on the development of an inspection satellite using

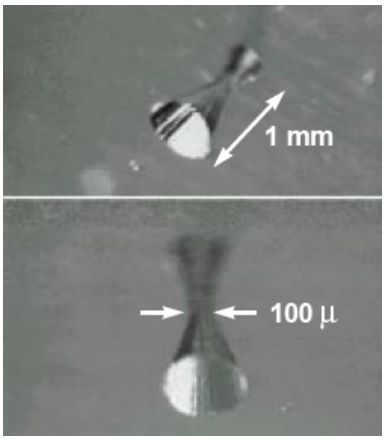

Figure 2.7 Nozzle realized by laser exposure of Foturan [Janson, S.W. and Helvajian, H., 1999]

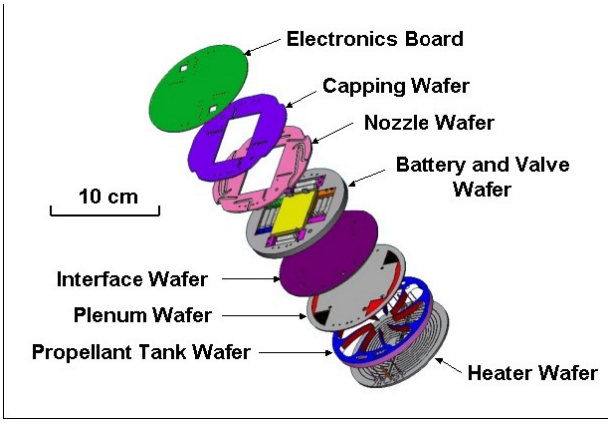

Figure 2.8 Solidworks representation of the propulsion module [Janson *et al.*, 2005]

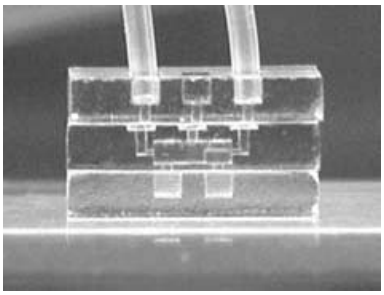

Figure 2.9 Microvalve [Sugioka, K. *et al.*, 2005]

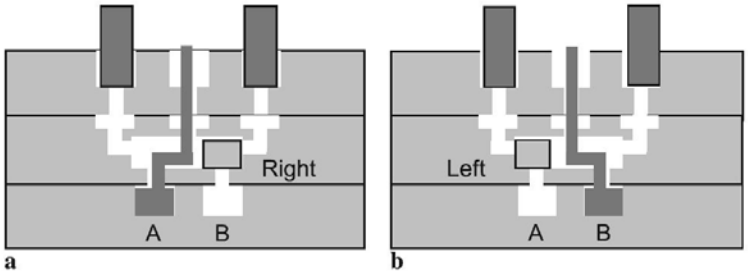

Figure 2.10 Scheme of the micro-valve [Sugioka, K. *et al.*, 2005]

Foturan [Janson, S.W. and Helvajian, H., 1999]. The propulsion module is composed of seven layers in Foturan material. Figure 2.8 shows a Solidworks representation of the propulsion module. Janson demonstrated one-axis positioning control with the propulsion module on an air table system.

A group from the RIKEN Institute in Japan has reported on the fabrication of a micro-valve in Foturan (Figures 2.9 and 2.10). A movable glass piece is located inside the glass to activate the valve [Sugioka, K. *et al.*, 2005]. The thickness of the substrate containing the micro-valve amounts to $5mm$.

Figure 2.9 shows an example of a microstructure machined under the surface of Foturan. Two aspects have to be considered within the process of fabricating such structures. First, the process needs intensity greater than the threshold value [Hongo *et al.*, 2005]. Second, the laser beam focussing optics has to have a high numerical aperture. When the laser beam is focused inside the glass, with its intensity at the focal point exceeding that of the threshold value, it becomes possible to machine the glass without affecting its surface.

CHAPTER 3

CHALLENGES, OPPORTUNITIES AND OBJECTIVES

3.1 Challenges

Glass, as a material, appears to be very useful for the fabrication of lab-on-a-chip devices. It possesses a lot of advantages in comparison to plastics such as chemical stability and a good mechanical resistance [Dietrich, T.R. *et al.*, 1996, Karnakis, D.M. *et al.*, 2005, Kim *et al.*, 2004]. Unfortunately the machining of glass still poses a number of challenges. For instance, the vast majority of machining methods produce a surface roughness which is not acceptable for photonic devices. Moreover, even if they produce a low surface roughness, they are usually unsuitable for prototyping. To my knowledge, only one machining method leads to low roughness while allowing rapid prototyping of devices: selective etching of photosensitive glass. This method requires photosensitive glass which was developed in the 1950s [Hongo *et al.*, 2005, Livingston, F.E. *et al.*, 2004]. The most widely used photosensitive glass is produced by *Schott Glass* under the trade name of Foturan [Sugioka, K. *et al.*, 2005].

Nanosecond excimer lasers emitting at 248 nm and 355 nm, and femtosecond lasers emitting at 775 nm are the main sources of light used for the irradiation within this approach. Unfortunately, femtosecond lasers are very expensive and excimer laser at 248 nm and 355 nm give a poor precision for the machining of surface layer.

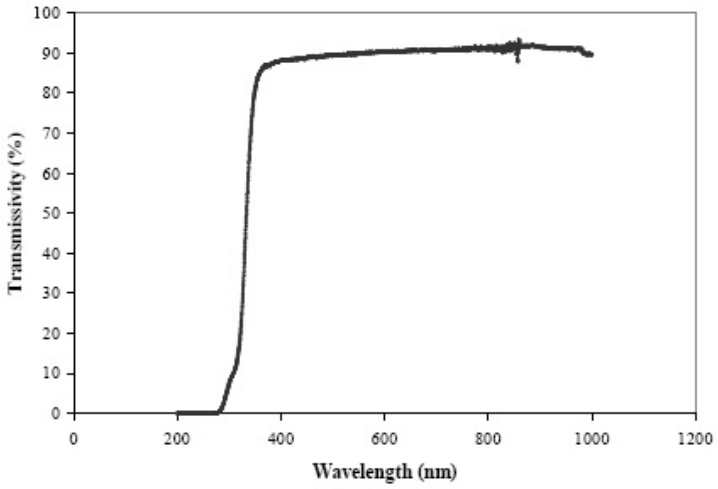

Figure 3.1 Spectral transmissivity of a 2mm thick Foturan sample [Fisette *et al.*, 2006]

3.2 Opportunities

In the frame of the here discussed research, it is proposed to investigate the machining conditions using an excimer laser at 193 nm, a wavelength used for the first time to realized this machining process.

Figure 3.1 shows the spectral transmissivity of a 2 mm thick Foturan glass [Fisette *et al.*, 2006]. As we can see, it has a higher absorption coefficient at 193 nm than for other wavelengths usually used in the machining process. Consequently, we can expect a greater gradient of laser intensity near the surface region of this glass. This greater gradient will probably allow a better control of etching depth as the etching depth strongly depends on the ability to control the depth of crystallization.

3.3 Objectives

The main goal of the project is to investigate micromachining of Foturan using 193 nm radiation for photoexposure. In particular, the following specific objectives will be pursued:

Determine critical dose of the 193nm irradiation for etching Foturan. The crit-

ical dose is the minimum laser energy that allows the creation of a sufficient concentration of lithium metasilicate to permit a selective etch.

Determine maximum depth of craters achievable with this approach. This will be achieved by controlling the laser irradiation dose (number of pulses and pulse fluence). The maximum etching depth is reached when an increase of the dose does not result in an increase of the etching depth.

Establish etch depth dependence on the total dose. The total dose is a combination of laser fluence and the number of pulses. Both parameters will be modified independently to know exactly the influence of each.

Determine profile (verticality) of etched craters. The verticality is defined by the angle between surface and the etching wall. The goal is to maximise this value.

Determine smoothness of processed surfaces. The surface smoothness is an important property to realize a photonic device. Consequently, the objective is to maximize the surface smoothness.

Investigate multi-step irradiation process. This objective concerns the repeatability of the machining process. The possibility to realize more than one-stage machining process gives a new tool for obtaining deeper structures.

CHAPTER 4

EXPERIMENTAL SETUP

This chapter presents the experimental setup that was used to fabricate and assess the machining process in Foturan. The first step of the machining process is the photo-exposure conducted with an ArF excimer laser (193 nm). For subsequent steps, furnace, wet bench and characterization tools are required.

4.1 GAUS laser station

The GAUS laser station was developed for photo-ablation machining. The laser station is described in the MSc thesis of Desbiens [Desbiens, 2006]. Figure 4.1 shows a diagram of the physical configuration of the laser station. The station components are described in table 4.1.

The laser (#1 on the figure) produced a laser beam at a wavelength of 193nm. Firstly, the laser beam crossed the shutters (#3) when they are open. After, two attenuators (#4, 6) adjust the laser power. The cross section shape of the laser beam is defined by a mask (#8) and finally, a focusing optics block permits a magnification of the image on the sample. The sample is positioned by three translation tables (#12, 13, 14) and one rotative table (#11).

This laser setup is not adapted for machining by the method described in this work. Consequently, some modifications are essential. With an approximated power value necessary for structuring by photo-exposition, we can adapt a micro-machining laser station. This station was designed for photo-ablation and the laser beam is consequently too powerful to be used. In fact, the photo-ablation of glass at 248 nm needs a fluence of about

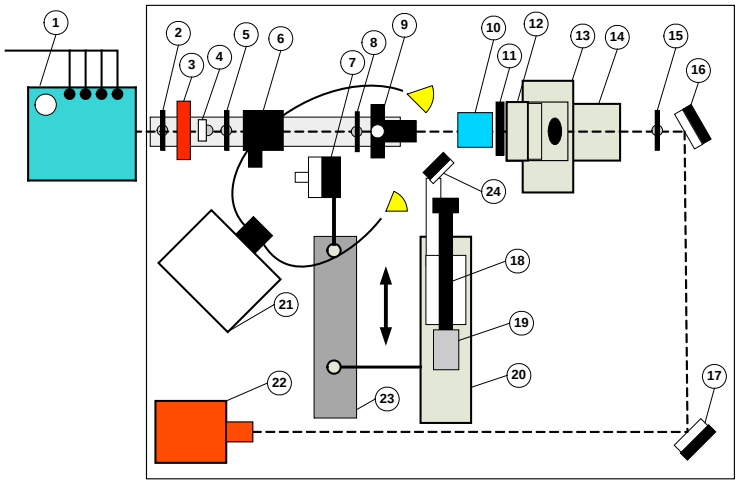

Figure 4.1 2D diagram of GAUS Laser station ([Desbiens, 2006])

Table 4.1 GAUS laser station description (adapted from [Desbiens, 2006])

#	**Description**	**Model**	**Function**
1	Excimer Laser	MPB Ximer 300	To produce UV laser beam ($193nm$)
3	Shutter	Uniblitz	To block temporarily the laser beam
4	Fixe attenuator	Edmund	To block 70% of laser beam
6	Variable attenuator	Metrolux ML2100	To control laser fluence delivered to the sample surface
7	Gower meter	Molectron	To measure the laser intensity
8	Mask	Melles Griot	To define the shape of laser beam
9	Focusing optics	Home made	To focus the laser beam
10	Sample holder	Home made	To support the sample during irradiation
11	Rotation table	Newport PR50CC	To rotate the sample
12	Translation stage (axis Y)	Newport ILS50CC	To move the sample along Y direction
13	Translation stage (axis X)	Newport ILS50CC	To move the sample along X direction
14	Translation stage (axis Z)	Newport ILS50CC	To move the sample along Z direction
18	Objective	Melles Griot	To project mask images on the sample surface
19	Digital camera	Sony DFW-SX900	To permit the visualization of machined surface
20	Translation table (visualization system)	Newport ILS250CC	To move the visualization system
21	Lighting by optical fiber	Stocker Yale Mille LUCE	To illuminated the sample
22	Helium-Neon Laser	Research Electro-Optics	Laser for optical path alignment

$0.5 J/cm^2$ [Talkenberg *et al.*, 2002]. This is 5 orders higher than the value necessary for the process we study.

The laser station of GAUS (Groupe d'Acoustique de l'Université de Sherbrooke) described by Desbiens [Desbiens, 2006] is adjustable in power. This is possible with some components, like a variable attenuator with its minimum transmissibility of 5% [Desbiens, 2006] and a fixed attenuator with a transmissibility of 30% [Desbiens, 2006]. Consequently, the micro-machining station permits an attenuation of 98.5%. Unfortunately, this is still 1,500 times too high for machining by photo-exposition.

Nowadays, the beam shape is defined by a 3mm diameter circular mask. With modifications on this mask, we also modify the transmissibility. The final choice is a circular mask with a diameter of 1mm. The transmissibility of the latter is 7.7% compared to 68% for the 3mm mask [Desbiens, 2006]. This value (7.7%) is estimated with the measure of transmissibilities for different laser beam power.

Finally, utilization of an exposition diameter of 1mm, in comparision with $35\mu m$ used previously, permits us to obtain the right fluence. With this modification, the minimal fluence possible is situated below the theoretical threshold value for photo-exposition. All these modifications permit an attenuation which is 5000 times lower than initially delivered by this system.

In addition to physical modifications, we also have to improve the software of the micro-machining station. This is necessary in order to control the number of pulses for the exposition. The new unit can calculate the time of exposition in function of the pulsation rate and the number of pulse wanted. Moreover, it permits real-time control of the shutter.

The main problem with this system is that it has not been designed for mask projection lithography: a technique that was explored with the QS Group laser processing station.

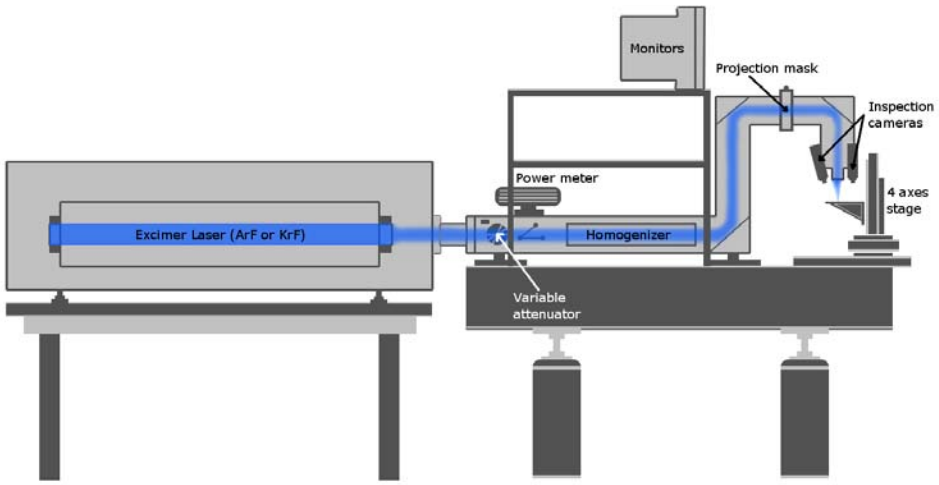

Figure 4.2 2D sketch of the QS Group laser station [Shaffer, E, 2007]

4.2 QS Group laser station

This second laser station was principally used for the experiment. This laser system was designed to allow exposure of special masks on the sample surface. Its side view is shown in Figure 4.2.

4.2.1 Excimer laser

The laser is illustrated at left on the Figure 4.2 and Figure 4.3 shows a picture of them. This excimer laser is fabricated by GSI Lumonics. It is principally used at a low pulse repetition rate, under 20 Hz. This laser has a pulse energy of $230mJ$. The pulse duration (FWHM) (**F**ull **W**idth at **H**alf **M**aximum) is about $12ns$. The pulse-to-pulse stability of power was measured to be $\pm 10\%$.

Table 4.2 QS group laser station description

Description	**Model**	**Function**
Excimer Laser	GSI Lumonics PulseMaster PM-846	To produce UV laser beam ($193nm$)
Variable attenuator	JPSA	To control laser fluence delivered to the sample surface
Power meter	Gentec Wv-330VUV	To measure the laser intensity (pulse fluence)
Homogenizer	JPSA Fly Eye	To homogenize the laser beam
Projection mask	JPSA custom made	To define the shape of laser beam
Inspection cameras	Panasonic WV-BP332	To permit the visualization of machined surface
Translation stage (axis Y)	Newport ILS150CC	To move the sample along Y direction
Translation stage (axis X)	Newport ILS150CC	To move the sample along X direction
Translation stage (axis Z)	Newport ILS50CC	To move the sample along Z direction
Rotation stage	Newport PR50CC	To rotate the sample
Focusing objective	Home made	To project mask image on the sample surface (demagnification of 2.6)
Sample holder	Home made	To support the sample during irradiation

4.2.2 Variable attenuator

In the optical path, the first part crossed by the laser beam is the variable attenuator made by JPSA. The operating principle is based on changing the transmission of a multi-layer dielectric coated plate that is rotated in front of the laser.

4.2.3 Beam homogenizer

The second part in the optical path of the laser beam is a beam homogenizer. Figure 4.5 show the operation principle. Firstly, the beam is separated in many small laser beams. All these sub-beams are re-focused to a single beam. The beam homogenizer is a base for the realization of the excimer laser mask projection technique.

4.2.4 Projection mask and converging lens

An image of any shaped 2D mask can be projected with a demagnification ratio of 2.6. The masks principally used for this experiment had square or rectangular shapes. These shapes were selected for the simplicity of measuring profiles of the fabricated craters.

Figure 4.3 QS Group excimer laser

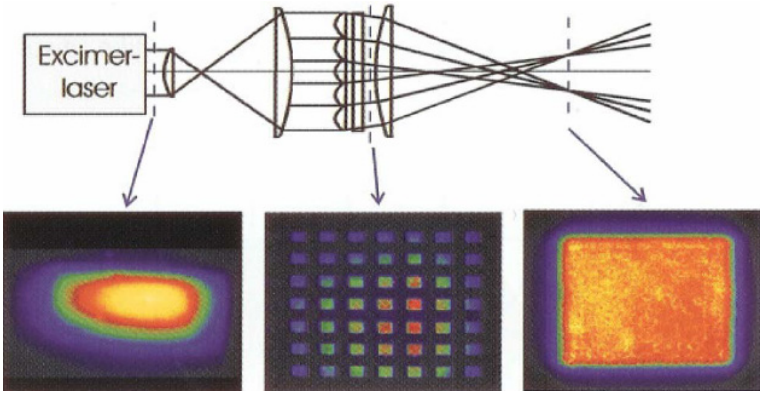

Figure 4.4 Operation principle of a beam homogenizer [Dubowski, 2005]

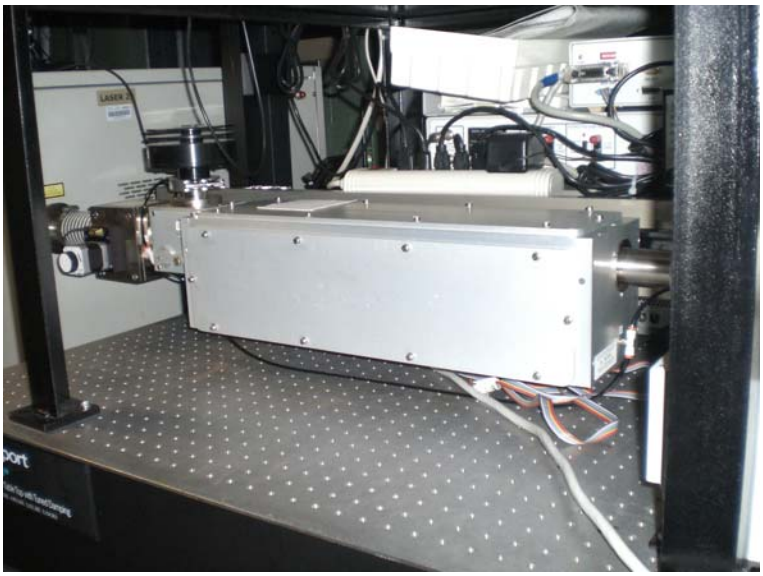

Figure 4.5 Beam homogenizer on QS group laser station

Moreover, a special mask depicting a contour of the maple leaf, which is shown in Figure 4.6, was used for some experiments.

4.2.5 Sample holder

The position of samples is controlled with a four-axis (X-Y-Z-Theta) system. Figure 4.7 shows the configuration of a sample holder and positioning system. This positioning system is controlled with a computer interfaced with the X-Y-X-Theta driver.

4.3 Furnace

A furnace is needed for the second step of the machining process. This furnace has to be programmable and able to reach a temperature of $605°C$. The furnace used within this project is the $3-550$PD Vulcan Model. The main features of this furnace are:

- Operating temperature range: $50°C$ to $1100°C$
- Linear temperature rates range: $0.1°C/min$ to $40°C/min$.

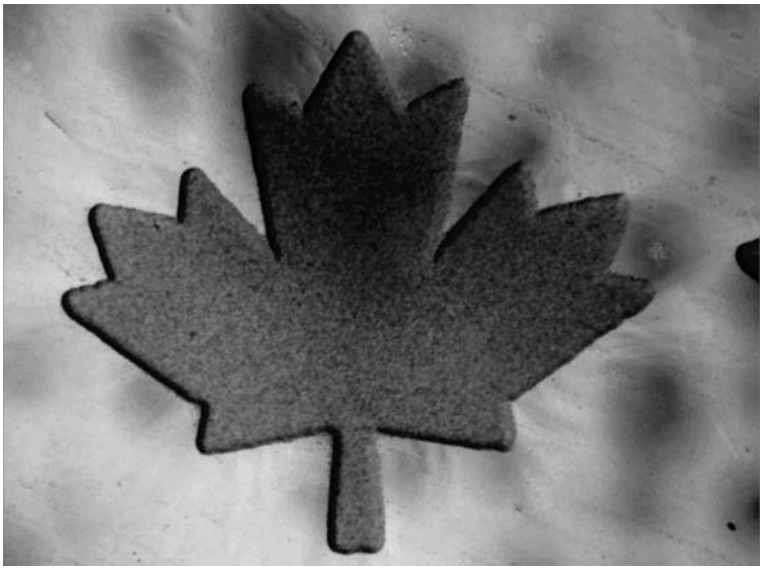

Figure 4.6 A 'Maple leaf' crater etched in Foturan

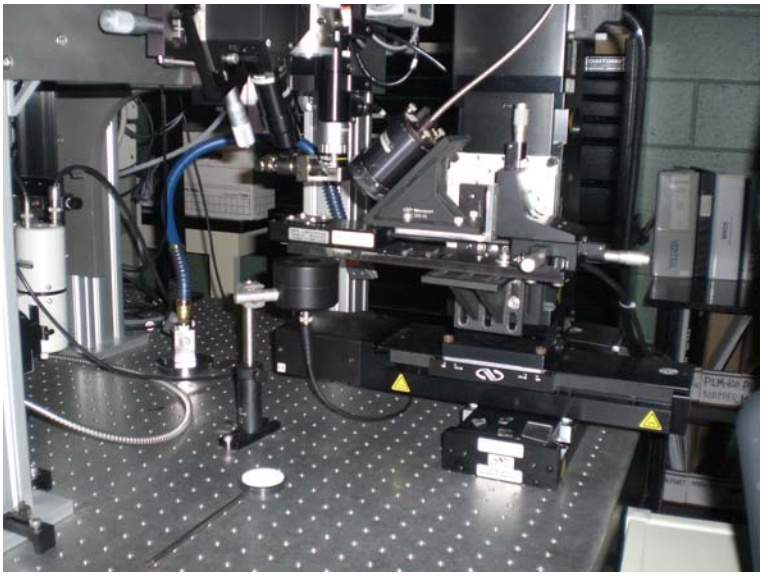

Figure 4.7 System for 3D positioning of sample on Qs group laser station

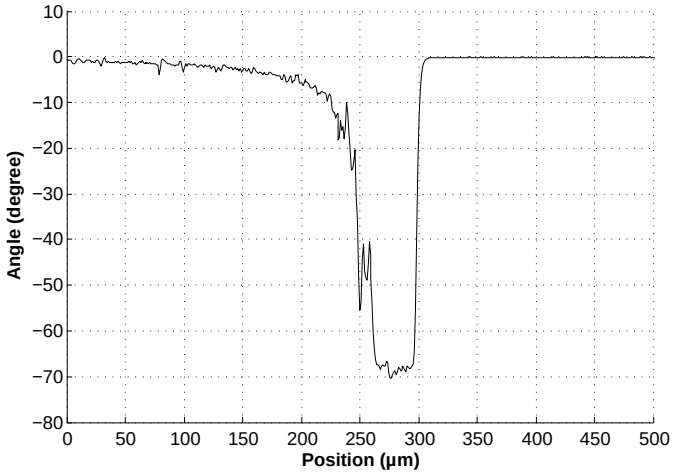

Figure 4.8 Maximum angle measurable by profilometer

The furnace has been equipped with a system allowing to flush the sample with inert gas (Nitrogen) during the annealing procedure, which provides a clean environment and prevents surface oxidation.

4.4 Characterization tools

A profilometer is used to measure the roughness, the etching depth and allows us to compare qualitatively the shape of the craters. The achievable resolution is $2.5nm$ and the stylus has a diameter of $5\mu m$.

Figure 4.8 show the angle measurement by the profilometer for one of the samples. The tip follows the surface and the end of sample is reached at about $200\mu m$. Due to the stylus diameter, the accurate measurements are obtained for angles inferior to 70°.

CHAPTER 5

PROCESS CHARACTERIZATION

Since micromachining by photo-exposure with 193nm excimer laser is examined for the first time, we used the results of 248nm and 355nm processing as a reference point. In particular, this concerned a threshold dose necessary to achieve machining. This threshold dose is a function of pulse fluence and the number of pulses, expressed by the relation [Fuqua, P.D. *et al.*, 2000, Hongo *et al.*, 2005]:

$$D_c = NF_c^m \tag{5.1}$$

where N is the number of shot, F_c the threshold fluence and m the power exponent.

5.1 Preliminary experiments

The preliminary experiments served to establish experimental conditions leading to micromachining of Foturan using the 193nm radiation. Some parameters, such as the strong absorption of the 193nm radiation by Foturan suggests that this approach should be feasible for fabrication of shallow microstructures. In addition, we investigated the influence of waiting time between the irradiation and the annealing steps on the microstructuring processes. We also studied a surface cleaning method to assure repeatable results.

Table 5.1 Laser fluence (mJ/cm2) and number of pulses examined with the preliminary experiment

#	**Fluence (mJ/cm^2)**	**Number of pulses**
1	0,012	300
2	0,012	1000
3	0,012	3000
4	0,012	10000
5	0,10	100
6	0,10	300
7	0,10	1000
8	0,10	3000
9	1,0	100
10	1,0	300
11	1,0	1000
12	1,0	3000

5.1.1 Validity of the process

A preliminary experiment was carried out using the GAUS laser setup (Section 4.1) to determine the threshold irradiation conditions and validate the process of micromachining. To estimate the threshold dose at 193nm, we compare the threshold doses for 355nm and 266nm, which are $9*10^4(mJ/cm^2)^2$ and $6*10^2(mJ/cm^2)^2$ respectively [[Fuqua, P.D. *et al.*, 2000]]. If we assume a logarithmic dependence of the critical dose on the wavelength, we can estimate a critical dose at 193nm as $10(mJ/cm2)^2$.

If we assume two-photon absorption process, in accordance to Equation 5.1 and with 1000 shots, we obtain a value of threshold fluence of $0.32mJ/cm^2$. The test was carried out to verify this value, as described in Table 5.1.

Figure 5.1 shows an optical microscope reflection image obtained for the sample irradiated under conditions described in Table 5.1. Each of the six rows of sites represent results obtained for nominally the same irradiation conditions. The brighter color (contrast) of the laser irradiated sites is due to diffused reflection of the rough surface created by preferential etching of lithium metasilicate crystals.

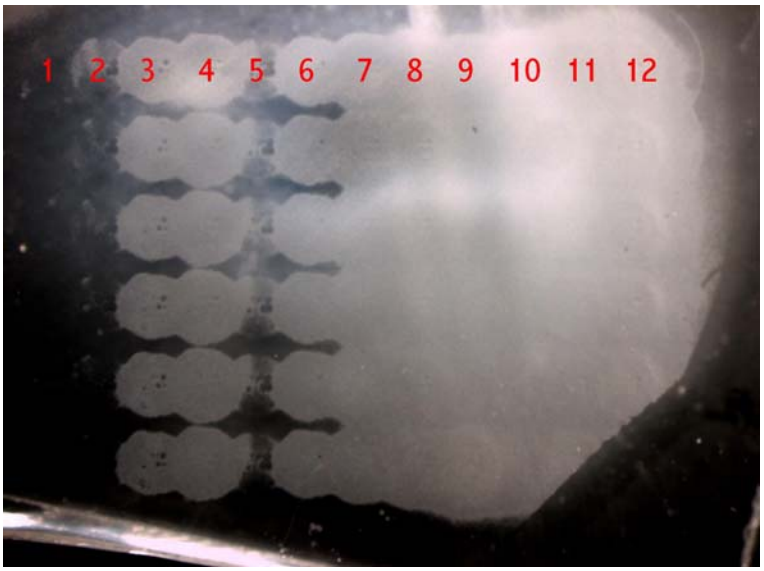

Figure 5.1 Optical microscope image of a Foturan sample irradiated with a $193nm$ laser at parameters listed in Table 5.1 (sites 1 to 12).

The first column of sites is not visible as the corresponding process parameters ($F = 0.012mJ/cm^2, N = 300$) were below the irradiation threshold. Thus, assuming that we have a two-photon process, we can estimate that a threshold dose, Dc, is greater than $0.043(mJ/cm^2)^2$ and inferior of $1(mJ/cm^2)^2$. This latter value is based on the results of column #5 ($F = 0.10mJ/cm^2$ and $N = 100pulses$).

Unfortunately, the laser workstation used for this experiment was not suitable for microfabrication of flat-bottom craters and, thus the estimated error in determination of the critical fluence is about 50%. Consequently, the results described in the following chapters have been obtained with the excimer laser workstation of the Laboratory for Quantum Semiconductors and Laser-based Nanotechnologies (QS Group).

5.1.2 Influence of the irradiation-annealing dwell time

The waiting (dwell) time between the photo-exposure and the annealing processes may influence the results as suggested by [Stillman *et al.*, 2007]. To address this issue, I have carried out a series of experiments for six sites on the same sample irradiated with nominally the same laser parameters, as shown in Table 5.2. These results were obtained with the QS Group laser.

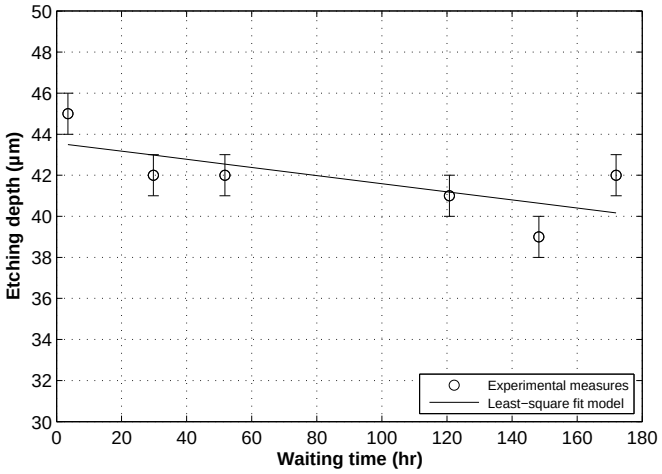

Figure 5.2 Influence of waiting time on etching depth

Figure 5.2 shows the variation of etching depth with the dwell time between photo-exposure and the annealing process. It can be seen that the depth of etched craters decreases with the dwell time. A least-square setting procedure gives the following time dependence for the depth of etched craters:

$$D[\mu m] = 43.6 - 0.02t[hours] \tag{5.2}$$

Table 5.2 Laser setting for experiment on dwell time influence on process

Fluence (mJ/cm2)	32
Pulse rate (Hz)	2
Number of pulse	100

From this experiment, I estimate that the maximum depth of etched craters decreases approximately by $2\mu m$ for each hundreds of hours of the dwell time. Thus, to avoid the influence of this effect on the results, we carried out all the experiments with the dwell time inferior to 24 hours.

5.1.3 Annealing condition

Section 2.2.4 described the temperature ramp for the second stage of the process (annealing) following the information available from literature. It has also been reported that after the annealing procedure, the samples required polishing to achieve an optical surface finish. We investigated the influence of the atmosphere during the annealing procedure on surface morphology of etched samples.

Using an optical microscope, we observed that the surface of the amorphous phase glass gives specular reflection, while that of the crystalline phase (following irradiation and annealing) gives a diffusive reflection.

The likely reason for this difference is the appearance of a modified layer of material developed at the surface during the heat treatment. After HF etching, this layer forms a rough surface. To address this problem, the following annealing treatment test was made under a nitrogen environment. This environment permit to concentrate the crystalline phase formation on the irradiated surface.

5.1.4 Saturation regime

As described in more details in the following chapter, the etching depth increases with increasing dose of irradiation. When a specific dose is reached, the relation between total dose and etching depth changes and the etching depth became independent of total dose. The dose for which this relation takes place is called the saturation dose.

The test elaborated to evaluate the value of the saturation dose was carried out for the pulse fluence of $42mJ/cm2$ and nine different values of number of pulses from 10 to 2000. Figure 5.3 shows the etching depth as a function of number of pulses (total dose). It can be seen that the saturation is achieved for 500 shots. This mean that for a fluence of $42mJ/cm^2$ the maximum etching depth is about $35\mu m$.

An other sign of saturation is the peripheral zone of the crater. With a dose superior to the saturation dose, the limit between crater and glass surface is unclear. Figure 5.4 shows this phenomenon. We can see the shape of the saturate crater, but they have diffuse

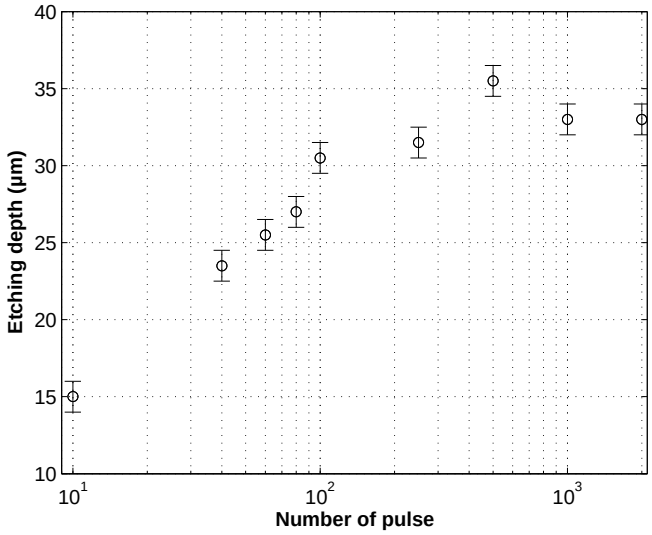

Figure 5.3 Etch depth dependence on the number of irradiating pulses at $42mJ/cm^2$

reflection in proximity of this crater, sign of glass etch.

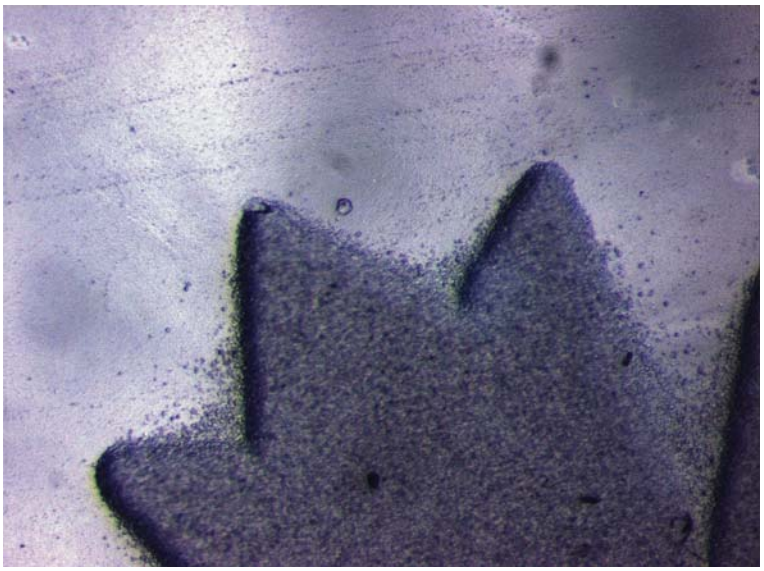

Figure 5.4 Optical microscope view of a saturated crater

5.2 Process parameters

To anticipate adequately the profiles of etched craters, we have to know the etch rate dependence on laser fluence and the irradiation dose.

Figure 5.5 Definition of the angle between the original surface and the etched wall (α)

5.2.1 Verticality of etched craters

The verticality of etched craters is defined by the wall etching angle. This angle consists of the angle between the side of the crater and the horizontal surface as defined in Figure 5.5.

5.2.2 Dose

The dose combines fluence and number of pulses. To evaluate the effect of the pulse fluence on the etching depth, we have carried out a test for different number of pulses and fluences as described in Table 5.3. The first two stages (photo exposure and heating) of the process were followed by chemical etching of 10% of HF for five minutes.

Table 5.3 Laser settings for experiment on influence of laser fluence and number of pulses on etching depth.

Fluence (mJ/cm2/pulse)	Number of shot
10	[1,2,4,6,8,10,12,15,20,30,50]
20	[1,2,4,6,8,10,12,15,20,30,50]
30	[1,2,4,6,8,10,12,15,20,30,50]
50	[1,2,4,6,8,10,12,15,20,30,50]
100	[1,2,4,6,8,10,12,15,20,30,50]

Figure 5.6 shows the dependence of the etching depth on laser fluence for different number of pulses. We observed a linear dependence of the etching depth with respect of $Ln(F)$. Moreover, the slope is the same for all pulse number. This observation indicates the independence of influence of both parameters (number of pulse and fluence) on the etching depth. This indepence can be represented by the following equation:

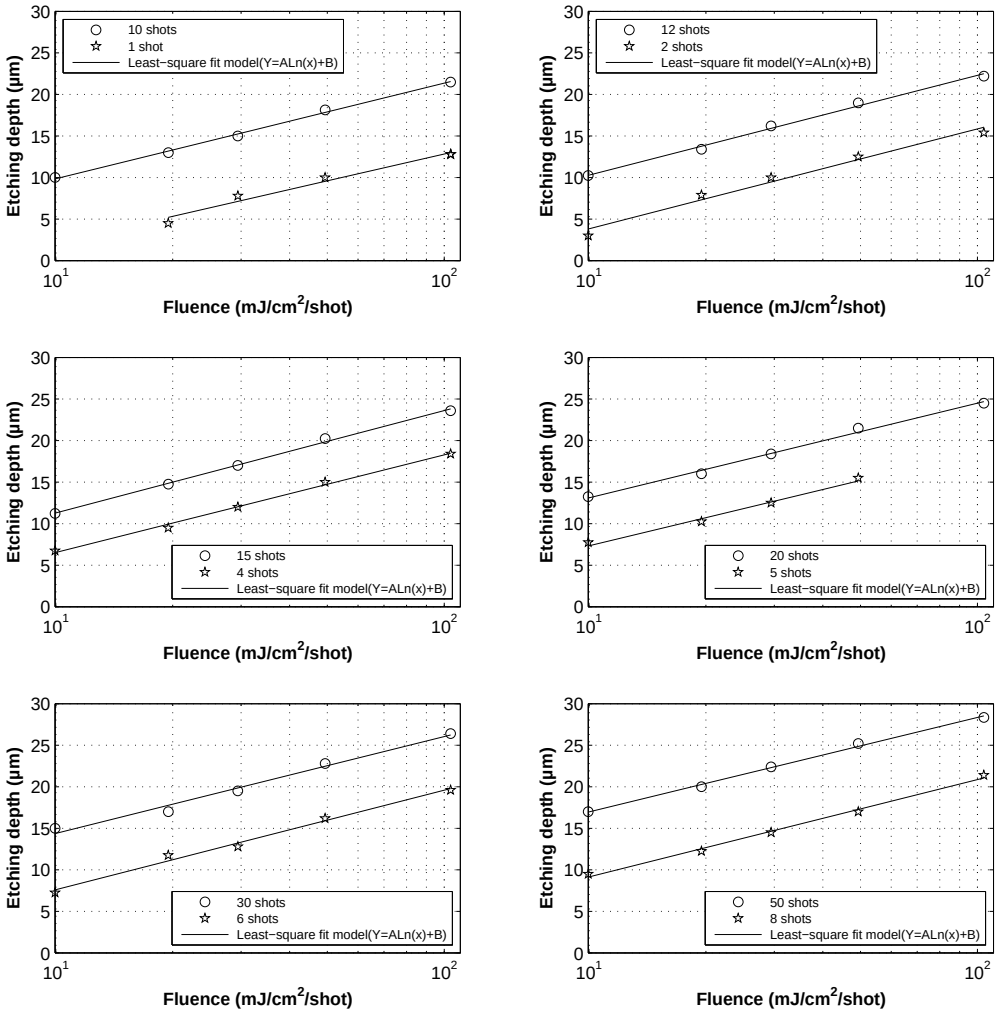

Figure 5.6 Dependence of the etching depth on laser fluence for different number of pulses

$$d(F,N) = f_1(F) + f_2(N) + A_3 \tag{5.3}$$

where f_1, f_2 and A_3 are respectively a function of the fluence, a function of the pulse number and a constant. The linear tendency between etching depth and $ln(F)$, shown in figure 5.6, permit to evaluate the value of the function $f_1(F)$.

$$d(F,N) = A_1 Ln(F) + f_2(N) + A_3 \tag{5.4}$$

where A_1 is a constant. After, the partial derivative of etching depth with respect of $Ln(F)$ is made:

$$\frac{\partial(d(F,N))}{\partial Ln(F)} = \frac{\partial(A_1 Ln(F) + f_2(N) + A_3)}{\partial Ln(F)} \tag{5.5}$$

$$\frac{\partial(d(F,N))}{\partial Ln(F)} = A_1 \tag{5.6}$$

The value of this constant is determined with the figure 5.6. The slope of these curves gives us the value of A_1. The value of the constant is replaced in the equation 5.4.

$$d(F,N) = 5.0 Ln(F) + f_2(N) + A_3 \tag{5.7}$$

Figure 5.7 shows the evolution of etching depth as a function of the number of pulses. Etching depth shows a linear tendency with respect of $Ln(N)$. The slope is the same for all fluence values. This observation confirms the one made earlier about the independence of influence of both parameters. This linear relation for the influence of pulse number is added to equation 5.7:

$$d(F,N) = 5.0 Ln(F) + A_2 Ln(N) + A_3 \tag{5.8}$$

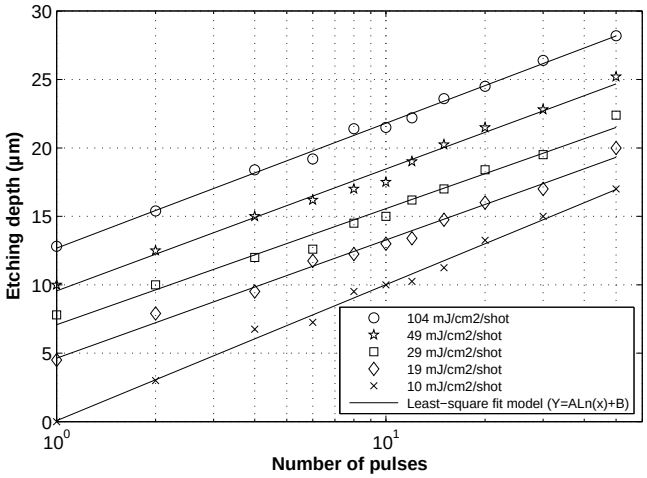

Figure 5.7 Dependence of the etching depth on the number of pulses for different pulse fluences.

The partial derivative in respect of $Ln(N)$ is made:

$$\frac{\partial(d(F,N))}{\partial Ln(N)} = \frac{\partial(5.0Ln(F) + A_2Ln(N) + A_3)}{\partial Ln(N)} \tag{5.9}$$

$$\frac{\partial(d(F,N))}{\partial Ln(N)} = A_2 \tag{5.10}$$

The value of this constant is determined with the Figure 5.7. The slopes of the curves gives this constant and is 3.9.

$$d(F,N) = 5.0Ln(F) + 3.9Ln(N) + A_3 \tag{5.11}$$

Then, the value of A_3 is determined. To do so, the error between the measured and theoretical estimate is minimized, the error being defined as the standard deviation:

$$\epsilon = \sqrt{\frac{\sum_{i=0}^{m}(d_{exp_i} - d_i)^2}{m}} \tag{5.12}$$

where d_{exp_i} is the measure of etching depth and d_i the value of etching depth from

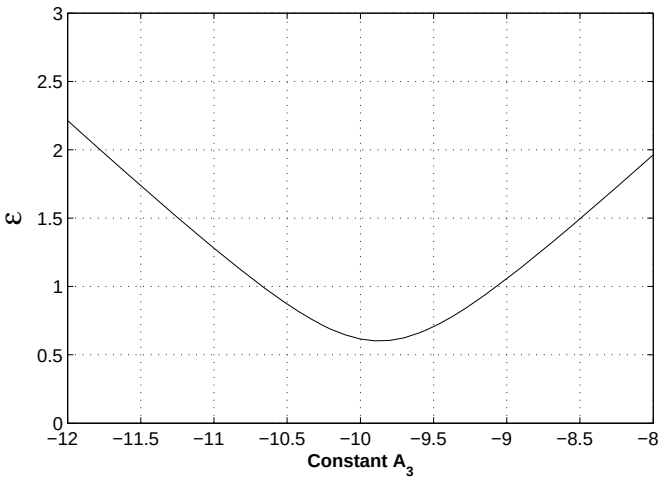

Figure 5.8 Standard deviation of equation 5.11

equation 5.11 for crater i. Figure 5.8 shows the relationship between ϵ and A_3. From this figure, we estimated the value of A_3 for minimum value of ϵ and it is included in equation 5.11:

$$d = 5.0Ln(F) + 3.9Ln(N) - 9.9 \tag{5.13}$$

This relation is valid below the saturation regime, i.e., $N \leq 500$ *pulses*. Gives the values of A_1, A_2 and A_3, the standard deviation of this equation is 0.6023, as shown in figure 5.8. The difference between measured etching depth (d_{exp_i} and predicted etching depth from equation 5.13 (d_i) is plotted in figure 5.9 for each crater i. It is shown that etching depth for almost all craters is correctly predicted by equation 5.13, within a confidence interval of 95%, corresponding to twice the standart deviation.

5.2.3 Etching time

Effect of etching time on etching depth

To measure the etching speed, we have carried out an experiment for three values of pulse fluences and numbers of pulses, as defined in Table 5.4. The experiment was carried out in a series of 30-second etching steps. After each step, the depth was measured with a

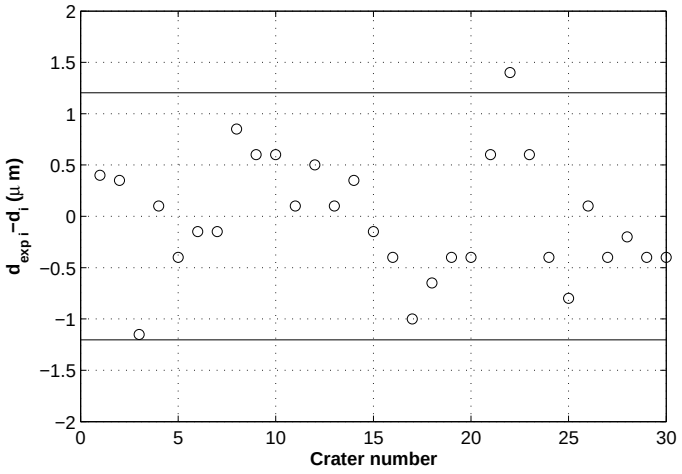

Figure 5.9 Error between the measurement and the estimated value with equation 5.13.

profilometer. Figure 5.10 shows the results for a fluence of $33mJ/cm^2$ and $N = 1$, 10 and 100 laser shots. In all cases, an "S" like shape dependence has been observed, with the saturation of the etching depth achieved for $4-5$ min of etching. This indicates the total removal of the crystalline phase of Foturan. No significant etching observed for $t < 90$ sec suggests the presence of an "incubation" effect that is required to begin the removal of material. The region between the onset of etching and the saturation shows a linear etching dependence with the etching speed estimated as $13\mu m/min$ for all irradiation doses.

Table 5.4 Effect of etching time on etching depth

Fluence (mJ/cm^2/pulse)	Number of shot
9.5	[1,10,100]
32.5	[1,10,100]
71.1	[1,10,100]

Figure 5.11 shows the dependence of etching depth on etching time for sites irradiated with 10 pulses at 10, 33 and 95 mJ/cm^2. An "S" like shape dependence, similar to that shown in Fig. 5.10, indicates that the same mechanism is responsible for material removal even for the relatively large pulse fluence of $95mJ/cm^2$.

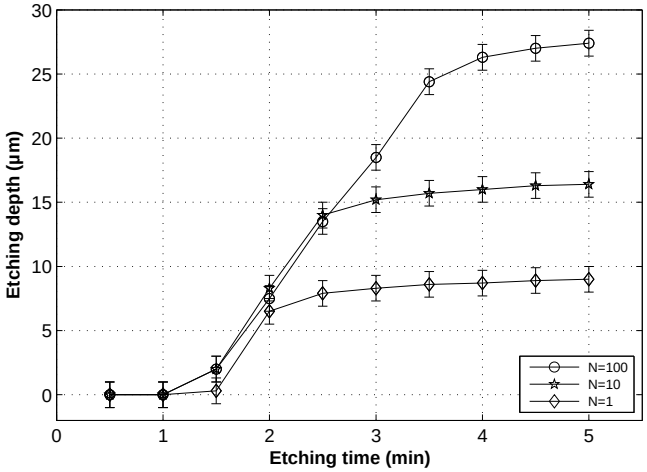

Figure 5.10 Dependence of the etching depth on etching time for different irradiation doses (pulse numbers) and same pulse fluence of $33 mJ/cm^2$.

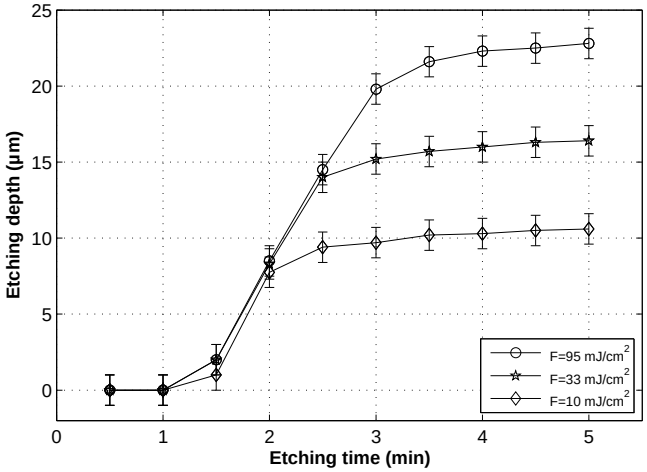

Figure 5.11 Dependence of the etching depth on etching time for sites irradiated with 10 pulses and different pulse fluences.

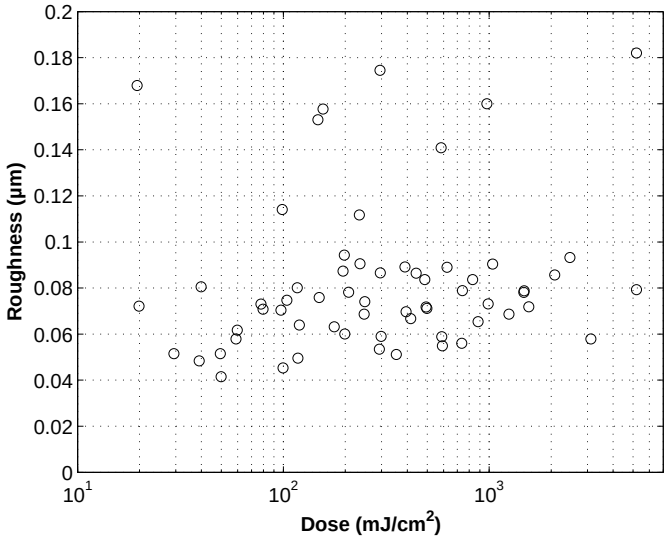

Figure 5.12 Effect of total dose on surface roughness

Effect of total dose on surface roughness

Figure 5.12 shows the relation between roughness of etched surfaces, as determined by a mechanical profilometer and the irradiation dose. These results have been obtained the etching time of 5 min.

In can be seen that, independently of the dose, the surface roughness varies between $0.04\mu m$ and $0.18\mu m$. Most points, however, indicate that roughness is below $0.1\mu m$.

Effect of total dose on the angle between surface and etched walls

The influence of dose on the angle between surface and etched walls, α, was studied for different pulse fluences and number of pulses adjusted independently. The results shown in Figure 5.13 were obtained for each point being an average of all angles measured for the same crater.

They can be described by the following logarithmic dependence obtained by implementing the least-square procedure:

$$\alpha = 4.2Ln(D) - 6.2 \tag{5.14}$$

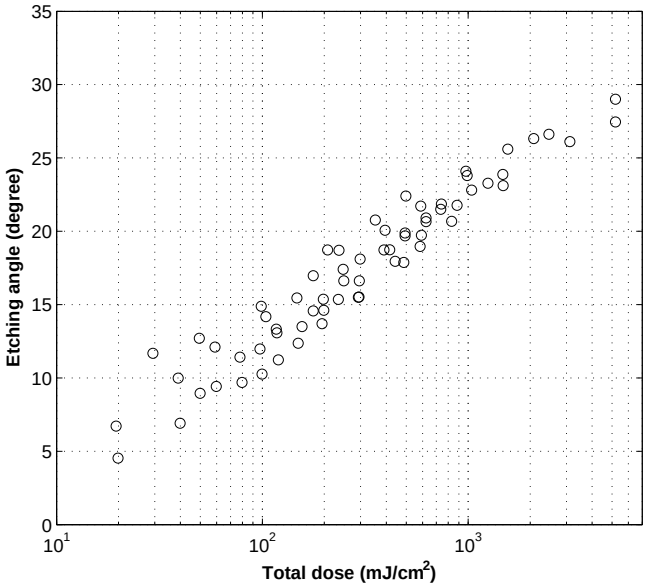

Figure 5.13 Effect of total dose on angle of etching

where α is in degree and D is the total dose in mJ/cm^2 . The agreement of this equation with the experimental data has been obtained for $R^2 = 0.9293$ (R^2 is the statistic coefficient of determination).

Figure 5.14 shows an example of a profile derivative measured for the $13\mu m$ deep crater that was fabricated following 5 min etching of the site irradiated with a total dose of $104mJ/cm^2$. (F = $104mJ/cm^2$, N = $1pulse$). This profile derivative was used to determine the etching angle.

Figure 5.15 shows the etching angle as a function of the etching time for a crater, which apart from the initial 2 points corresponding to the etching time $t < 90sec$, is saturated at near 50 deg. This crater is $26\mu m$ depth and was irradiated with a fluence of 27.5 mJ/cm^2 and 100 pulses. This result is about 20 deg better than one shows on Figure 5.13. This is explained by an increase of the quality of laser beam between both experiment. The component in the laser path was realign. This result in a better uniformity of laser fluence in the center and a better definition of laser beam. This shows that the laser beam quality has a strong influence on the etching angle.

We note that, ideally, α should be close to 90 deg. This, however, is expected to be strongly dependent on the intensity distribution of the laser beam used for the irradiation

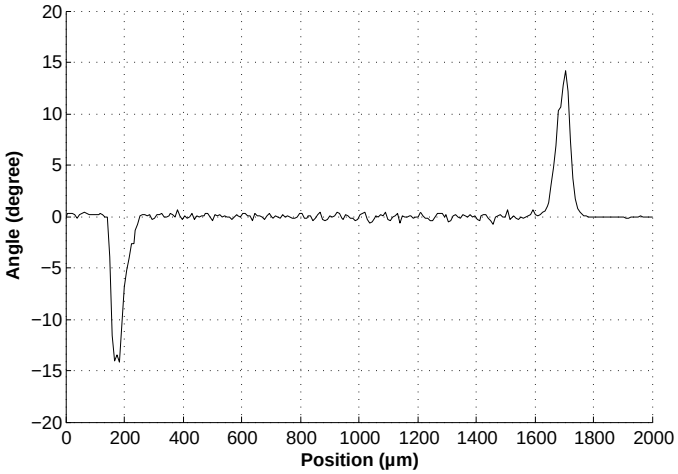

Figure 5.14 Derivative of a crater profile

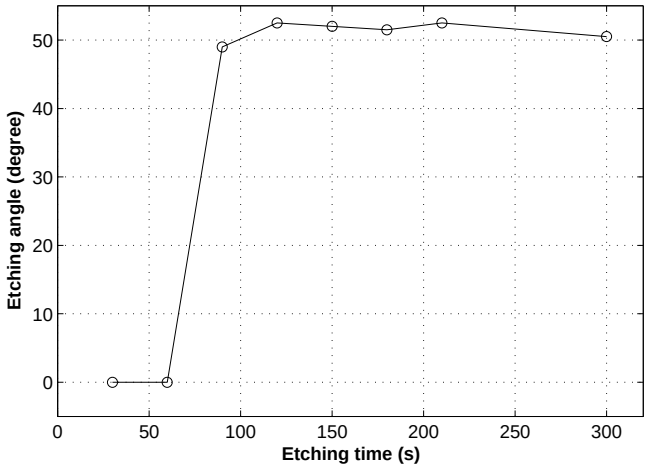

Figure 5.15 Effect of etching time on angle of etching wall

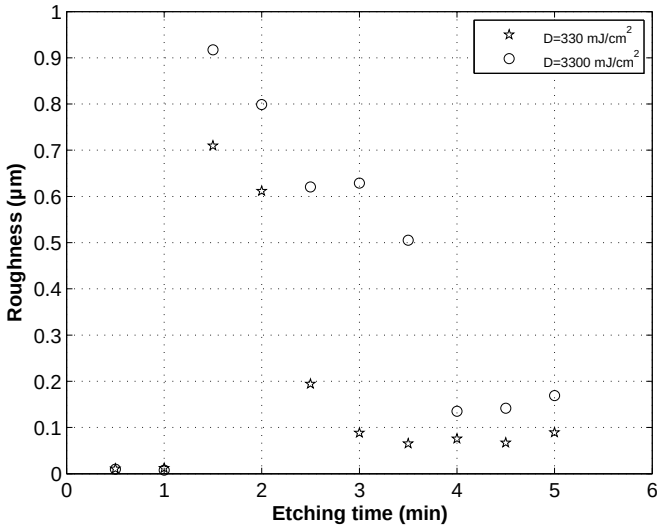

Figure 5.16 Effect of etching time on surface roughness

of the mask. More studies are required to address this issue.

Effect of etching time on surface roughness

Figure 5.16 shows the evolution of the surface roughness during an etching of 5 min for irradiation doses of 330 and $3300 mJ/cm^2$ ($F = 33 mJ/cm^2$, $N_1 = 10$ pulses, $N_2 = 100$ pulses) It can be seen that the amplitude of surface roughness increases radically in the first moment of etching. During the high speed etching ($t = 1.5 min$ to $3.5 min$), the surface roughness decreases moderately. When the structure achieve its final depth ($t = 4 min$), the surface roughness decreases rapidly. This indicates that the structure reached its final shape.

5.3 Multi-Step process

In accordance with our preliminary experiments concerning the irradiation of Foturan at 193nm, the maximum etching depth is lower than $35 \mu m$ (Section 5.1.4). To address the possibility of microfabricating deeper structures, we have investigated a multi-step process that consists of a repetition of the same three stages (exposure, annealing and etching). Figure 5.17 shows the profile of a microstructure obtained with a two-step process. Three

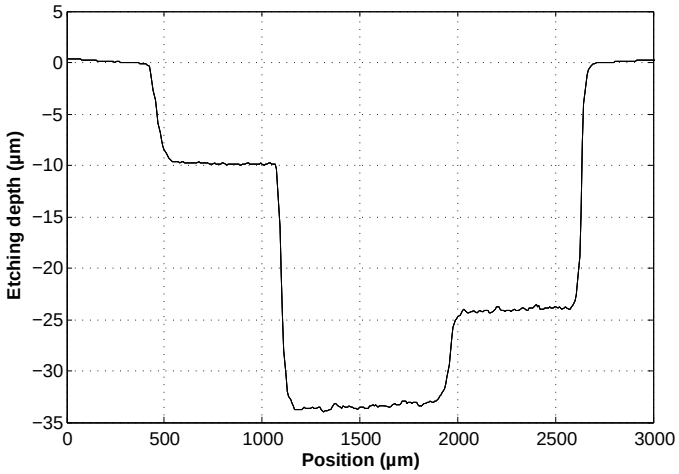

Figure 5.17 Profile of crater fabricated with a two-step machining process

plateaux can be easily distinguished in that figure. The first one ($500 < X < 1100\mu m$) is the result of the first exposure. The second one ($1100 < X < 2000\mu m$) is the result of both exposures. The third one ($2000 < X < 2600\mu m$) is the result of the second exposure. The conditions for the 1st and 2nd exposures were: $F1 = 10mJ/cm^2$, $N1 = 8$ and $F2 = 73mJ/cm^2$, $N2 = 35$, respectively. For these conditions, Equation 5.13 predicts 10 and $25\mu m$ deep craters, respectively. This compares with 10 and 24 deep craters that have been determined from the profile shown in Fig. 5.17. The second plateau have a etching depth of $34\mu m$ and it indicates a reasonable reproducibility of the process.

Figure 5.18 shows the evolution of the etched profiles measured for a $5 - step$ process that was carried out for consecutive irradiations at pulse fluences of 71, 57, 61, 100 and $135mJ/cm^2$ and number of pulses of 50, 60, 50, 50 and 100, respectively. It is interesting to note that this multi-step processing does not deteriorate significantly the morphology of the processes surface as the roughness of a $120\mu m$ deep crater is comparable to that of a $20\mu m$ deep crater. The deeper crater shows an exception, the bottom is none-uniform. The center is about $6\mu m$ upper than the side. Like this error is lower than 5% of crater depth, it is consider negligible.

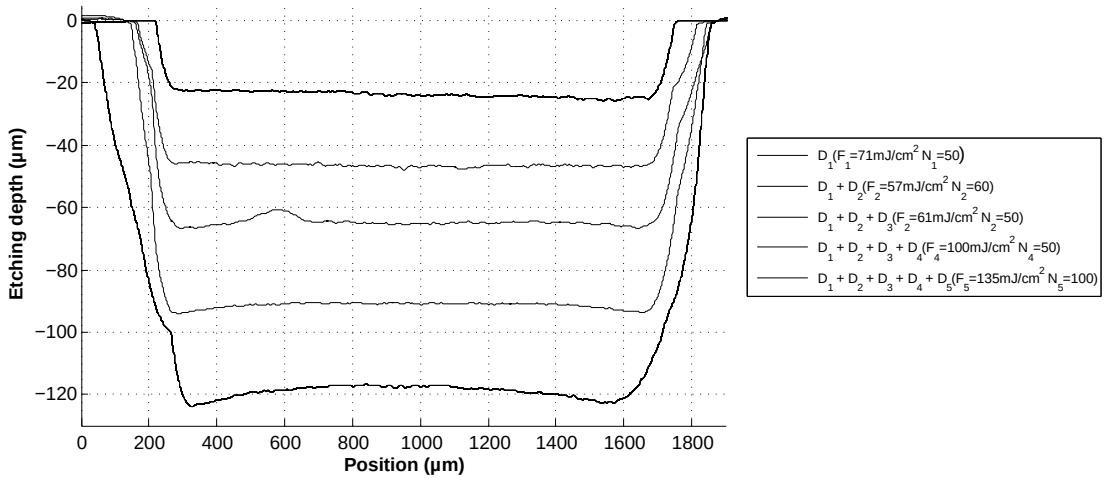

Figure 5.18 Profile of craters etched consecutively with a 5-step process

CHAPTER 6

DISCUSSION

This chapter presents an analysis of the $193nm$ absorption and threshold irradiation dose in Foturan. Understanding of these parameters is indispensable for the fabrication of multi-level (3D) structures fabricated during this project.

6.1 Absorption coefficient

The Beer-Lambert law gives the light intensity in material in function of depth x, absorption coefficient α, and light intensity on the surface I_0:

$$I(x) = I_0 e^{-\alpha x} [W/m^2] \tag{6.1}$$

The dose is the light intensity accumulated during a specific time. Consequently, a similar relation is used for the total dose:

$$D(x) = D_0 e^{-\alpha x} [J/m^2] \tag{6.2}$$

Let's assume that there is a dose threshold for crystallization. We can assume that the doses are similar at the interface of crystallization and amorphous glass phase for any irradiation. For irradiation doses D_1 and D_2, the crystallization depths are x_1 and x_2 respectively. The relation 6.2 becomes:

$$D_1 e^{-\alpha x_1} = D_2 e^{-\alpha x_2} \tag{6.3}$$

After some modification, we obtain:

$$D_1/D_2 = e^{\alpha(x_1 - x_2)} \tag{6.4}$$

We have two possibilities. The first one is with $N = cst$ and second one, with $F = cst$. For the first case, we make the assumption of $N = cst$ and we take two values of fluences, F_1 and $F_2 = XF_1$. With Equation 5.13, it is possible to calculate the etching depth for each dose:

$$d_1 = 3.9Ln(N) + 5.0Ln(F_1) - 9.9 \tag{6.5}$$

$$d_2 = 3.9Ln(N) + 5.0Ln(XF_1) - 9.9 \tag{6.6}$$

While replacing this in Equation 6.4, we obtain:

$$1/X = e^{\alpha(3.9Ln(N)+5.0Ln(F_1)-9.9-3.9Ln(N)-5.0Ln(XF_1)+9.9)} \tag{6.7}$$

With some simplifications, we obtain:

$$1/X = e^{\alpha(5.0(Ln(F_1)-Ln(XF_1)))} \tag{6.8}$$

$$1/X = e^{\alpha(5.0Ln(1/X))} \tag{6.9}$$

$$Ln(1/X) = \alpha(5.0Ln(1/X)) \tag{6.10}$$

While isolating α, we obtain an estimated Foturan absorption coefficient in glass at $193nm$:

$$\alpha = 1/5.0\mu m \tag{6.11}$$

$$\alpha_1 = 0.20\mu m^{-1} \tag{6.12}$$

The second possibility is to assume the constant fluence $F = cst$. With the same mathematical process, we obtained a second value for the absorption coefficient at $193nm$.

$$\alpha = 1/3.9\mu m \tag{6.13}$$

$$\alpha_2 = 0.26\mu m^{-1} \tag{6.14}$$

Table 6.1 shows the coefficient of absorption and the transmissivity of a $2mm$ thick Foturan for three wavelengths. For $\lambda = 193nm$, we use the mean value of $\alpha = 0.23\mu m^{-1}$. For other wavelengths, the value is take in the literature [Kim *et al.*, 2004, Livingston, F.E. *et al.*, 2004]. The transmissivity can be calculated from the equation:

$$T = I/I_o \tag{6.15}$$

where I is calculated using the Beer Lambert law. Thus the formula for transmissivity is given by:

$$T = e^{-\alpha x} \tag{6.16}$$

Table 6.1 allows to understand the limit of machining process Foturan using the $193nm$ irradiation. The $193nm$ radiation intensity decreases rapidly in the material, in contrast

Table 6.1 Absorption and transmission of Foturan for different wavelength

Wavelength (nm)	Absorption coefficient (μm^{-1})	Transmissivity (%) $40\mu m$ thick	Transmissivity (%) $2mm$ thick
193	0.23	0.01	≈0
248	0.023	40.7	≈0
266	0.001	96.1	13.5
355	0.000027	99.9	94.7

to 266 and $355nm$ radiation. For instance, to reach the threshold dose at a depth of $40\mu m$, the dose at the surface has to be 10000 times the threshold. Figure 3.1 [Fisette *et al.*, 2006], shows the transmissivity of a $2mm$ thick Foturan.

For known absorption coefficient, it is possible to calculate the light intensity at any depth using Equation 6.1:

$$x = \frac{-1}{\alpha} ln \frac{I_x}{I_0} \tag{6.17}$$

A measure of the cross section laser beam intensity was taken. For each position across the beam, we calculated the depth for an arbitrary intensity of machining threshold. Figure 6.1 shows line of machining threshold for different laser intensity.

We observed in Figure 6.1 an interesting property also observed experimentally. The angle between the surface and the etched wall increases when the etch is deeper, for the one step process only. The theoretical maximum etching angle is calculated for each specific intensity. To this, we calculate a numerical derivative of the depth profile. Figure 6.2 shows this evolution for the numerical model (solid line). The experimental measurements (circular dots) are also present on this figure. The experimental values are taken from the test about evolution of etching depth in function of laser fluence (Section 5.2.2).

The evolution of angle in the model is similar to the experiment. This indicates a reasonable validity of the model. The shift between reality and the model is principally attributed to the laser beam. In fact, the quality of the shape of the laser beam was improved between the etching experiment and the intensity profile measurement used for the model.

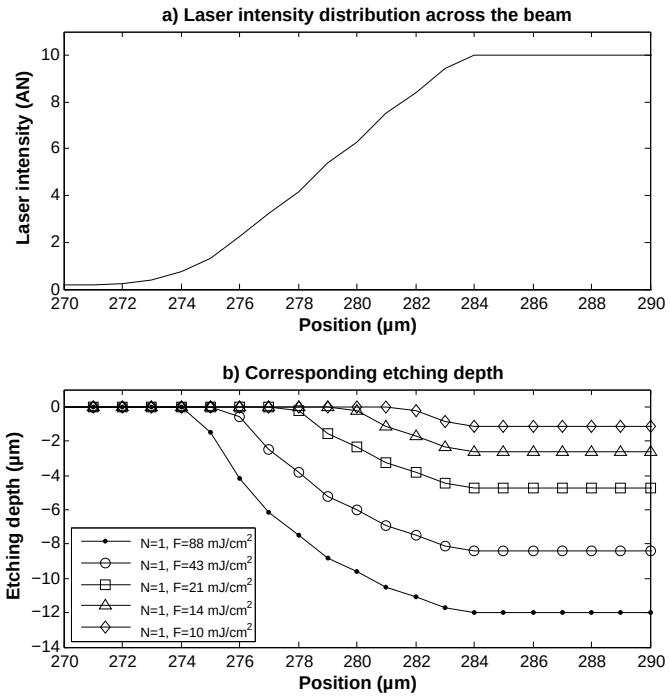

Figure 6.1 Numerical model to estimate the depth of threshold limit

6.2 Irradiation dose threshold

The evaluation of dose threshold is obtained with Equation 5.13:

$$d = 3.9Ln(N) + 5.0Ln(F) - 9.9 \tag{6.18}$$

The dose threshold happens when the etching depth is zero. When the relation gives a negative value, the dose is bellow the threshold. Therefore Equation 6.18 becomes:

$$0 = 3.9Ln(N) + 5.0Ln(F) - 9.9 \tag{6.19}$$

The equation is transformed to permit the relation of fluence threshold to be plotted in relation to the number of pulses:

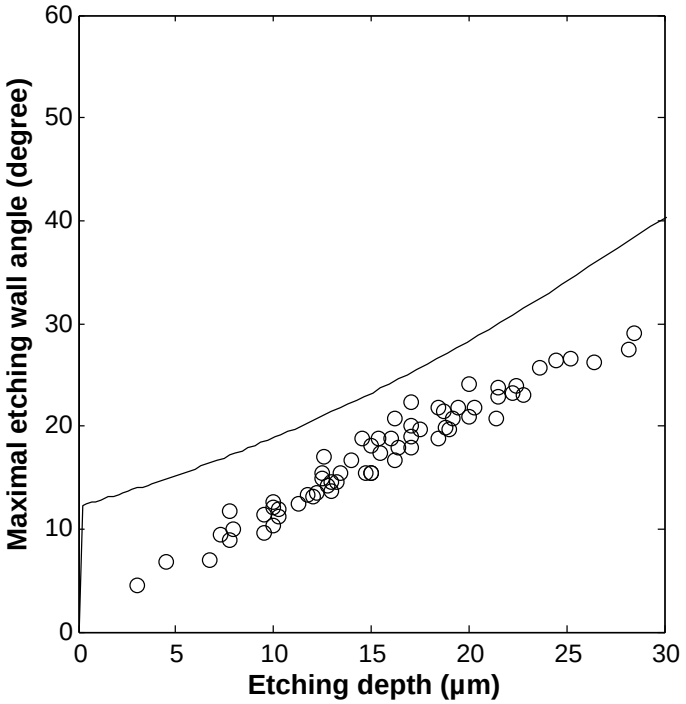

Figure 6.2 Relation between etching angle and etching depth, showing that the experiment result (o) and modeling predictions (-) have the same trend

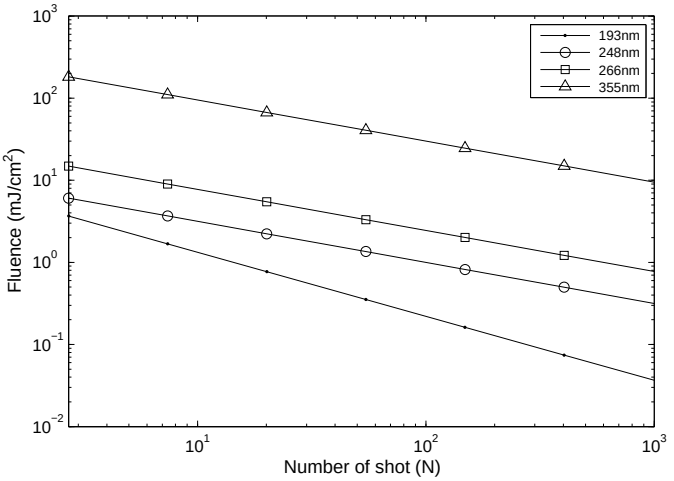

Figure 6.3 Evolution of fluence threshold in function of number of pulses for different wavelengths

$$F = e^{2.08-0.78Ln(N)} \tag{6.20}$$

With this equation, we can compare the threshold fluence for different wavelengths. Figure 6.3 shows this evolution and the values for others wavelengths are taken from the literature [Fuqua, P.D. *et al.*, 2000].

The difference in the slope is due to the power dependency. As described in Chapter 5, the threshold dose is proportional to the number of pulses and to the square of the fluence for other wavelengths. For $\lambda = 193nm$ the power is about $1,3$. Photons at $193nm$ are more energetic and result in a dose threshold inferior to others as illustrated in Figure 6.3.

6.3 3D microstructures with a movable mask technique

In this section, three multi level structures are presented. Two lenses (converging and diverging lenses) and a stair-like structure are presented.

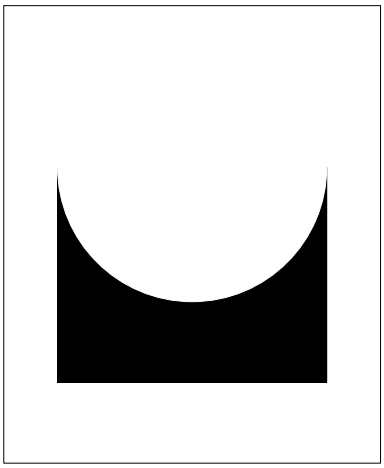

Figure 6.4 Mask for fabrication of a converging lens (The black section is the hole in the mask)

6.3.1 Converging lens

The first structure is a converging lens. The control on the etching depth is realized with the control of number of pulses. We profile the laser beam with the mask shown in Figure 6.4. The glass is moved under the laser beam. Consequently, the laser pulses is juxtaposed on the glass. This allows for multiple pulses absorbed in the glass where the mask is wider. The etching depth is control by the number of pulses absorbed by the glass. A profile of this lens is show in Figure 6.5.

For the moment, the lens has a high roughness. This is caused by the distance between two subsequent laser shots. To reduce the roughness, the next experiment will be realized with smaller distance between two laser shots.

6.3.2 Diverging lens

A second approach to realize multi-level structure with control on the number of pulses is to rotate the sample under laser beam. The beam shape is defined by a mask (Figure 6.6). The origin of cartesian coordinate system is the center of rotation of the mask. The shape is calculated to obtain a spherical lens. The equation which gives the etching depth (Equation 5.13) is taken into account for the elaboration of the shape of the mask.

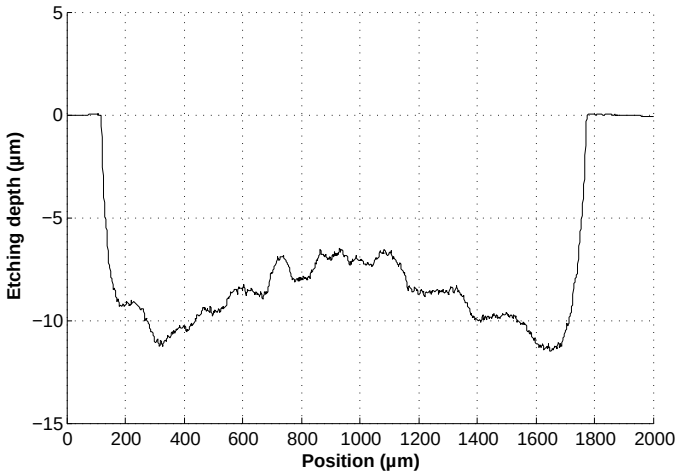

Figure 6.5 Profile of a converging lens

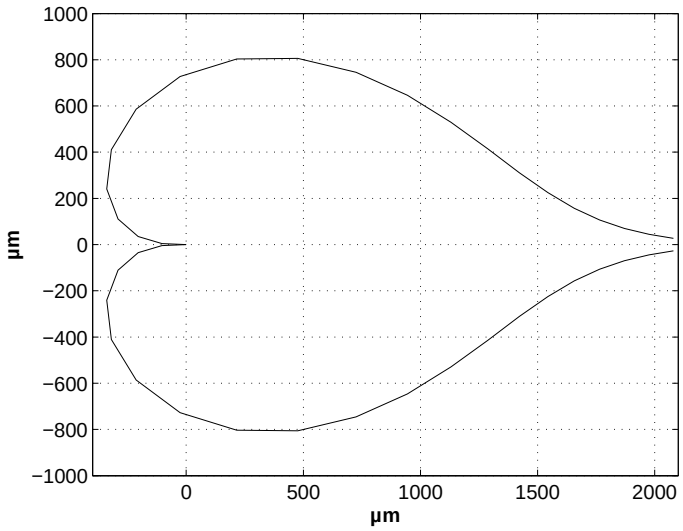

Figure 6.6 Mask for the diverging lens

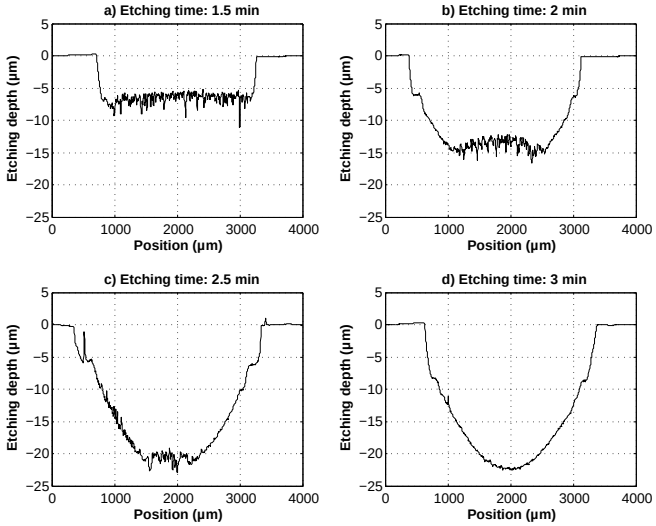

Figure 6.7 Profile of a diverging lens after increasing etch times

The result is shown in Figure 6.7. Moreover, the figure shows the evolution of etching depth from partial to final etching shape. The result on the evolution of roughness is visible on the partially etched profile.

6.3.3 Stair structure

Finally, we realized a stair-like structure. The multi-step procedure is used in this experiment. Figure 6.8 shows the laser spot. After each exposure, the sample was annealed and etched. The laser settings are shown in Table 6.2. The dose is about the same for each one.

Table 6.2 Laser setting for a stair structure

Exposure number	**Fluence** (mJ/cm2)	**Number of shot**
1	53	20
2	53	20
3	51	20

The result of this machining procedure is shown in Figure 6.9. This structure allows to show the repeatability of the process. For instance, we exposed three times the same dose and the etching depth is similar within an error of $1\mu m$.

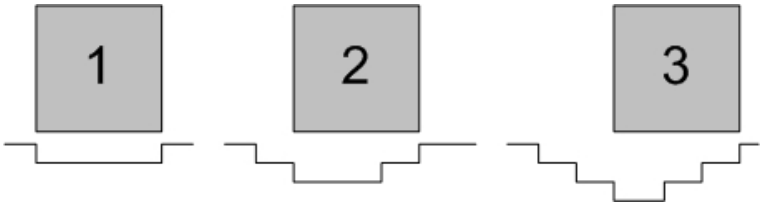

Figure 6.8 Irradiation conditions for a stair structure

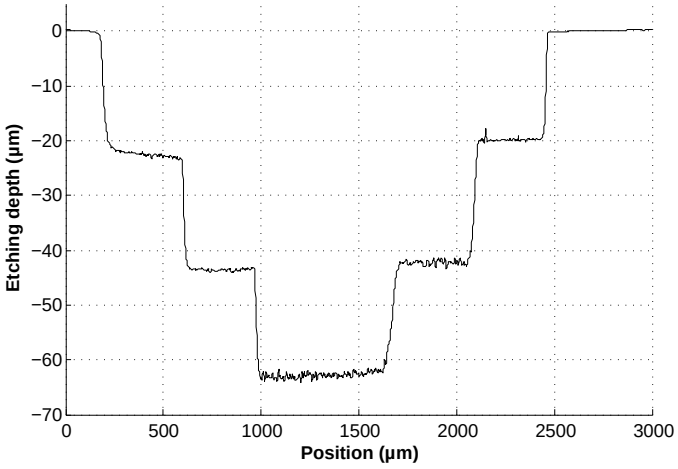

Figure 6.9 Profile of a stair structure

6.4 Things to know

This section presents the most important consideration for machining Foturan by the method described in this text at a wavelength of $193nm$.

The fluence threshold for Foturan is about 8mJ/cm^2 for one pulse.

The maximal etching depth is about 35μm. This limit is for one step etching exclusively.

Multi step is possible to create deeper structure than 35μm. Multi-step consists in a repetition of three first stage of machining process (Irradiation, annealing and etching)

The precision of the temperature during the annealing process is very important. A variation of temperature plateau of about 10° influences the etching speed and the shape of the crater.

The surface roughness of a partially etched structure is higher. The roughness can be used to evaluate if the etching is complete.

The sample has to be cleaned before irradiation. The surface properties are important to obtain repeatability. A non-uniform layer of dirtyness on the surface results in non-uniform etching. This is caused by the high absorptivity at $193nm$.

CONCLUSION

During this project, we investigated the machining of photosensitive glass with a laser ArF (193nm). As a first step, work on photosensitive glass made by other research groups has been analyzed. From this analysis, it appeared that there was an opportunity to improve machining surface. Thus, the choice was made on the ArF laser which emits at a wavelength of $193nm$. This wavelength is more energetic and is absorbed near the surface. This has the advantage to permit a better control of irradiation dose within the surface layer. Moreover, the influence of different machining parameters has been studied; the fluence and the number of laser pulses and the time of etching. They have both a logarithmic effect on the maximal etching depth. Then a method to machine deeper structures has been studied. This method consist essentially to achieve repeatedly the three stages of the machining method. For the moment, we achieved an etching depth four times deeper with this method but nothing indicates that the method cannot be repeated until the wanted depth is reached.

An analysis of experiments has permitted to evaluate equations that predict the etching depth of the crater produced. This relation predicts an etching depth with a fluence and the number of pulses used for the irradiation. This proved useful for making more complex structures. For example, the mask design is based on this equation. An example of these structures are diverging and converging lenses. The lenses do not have yet the required precision, but they demonstrate that this method of micromachining allows for structures with several levels. Finally, a series of techniques facilitating the use of this method have been proposed. This is to enable new users to pinpoint the problems in the event of failure of the method.

Some experiments and analysis carried out during this project were for the first time:

- Machining photosensitive glass with a ArF laser ($193nm$),

- Equation to predict the maximum etching depth with the fluence and the number of pulse,
- Multi-step process.

Thus, this micromachining method is interesting for structures made with glass. By combining with another method or with a different wavelength, it is possible to make more complex structures. This surface machining method could be combined with other UV lasers for machining volume. This machining method permits a better precision on the surface roughness compared to traditional photo-ablation. Moreover, the glass may explode when machined by photo-ablation. Finally, this method has an advantage over the selective etching DRIE for prototyping because it requires no complex mask.

Future work

Some items must now be clarified. First, we noticed an influence of the time between laser exposure and heat treatment on the etching depth. We were unable to determine precisely this influence, but a more precise study would clarify this point. Then, there is still some work to do on the $3D$ structures made to make them functional. A change in the mask of irradiation on the basis of the results of this master's work could give good results. Finally, it would be interesting to try the multi-step process by combining two wavelengths. For example, a circular cavity $30\mu m$ deep could be done with the ArF laser and a hole in the center of this cavity through the whole structure could be done with a wavelength of $355nm$.

REFERENCES

[Almaz Optics, 2006] Almaz Optics I. (2006) *SILICON Si.*

[An *et al.*, 2007] An R., Li Y., Liu D., Dou Y., Qi F., Yang H., Gong Q. (2007) *Optical waveguide writing inside Foturan glass with femtosecond laser pulses*, Applied Physics A (Materials Science Processing), vol. A86, no 3, p. 343–6, optical waveguide writing;Foturan glass;femtosecond laser pulses;femtosecond laser writing;femtosecond laser irradiation;refractive index modulation;minimum transmission loss;thermal treatment;optical splitter;pulse energy;.

[Bettiol *et al.*, 2006] Bettiol A., Venugopal Rao S., Teo E., Van Kan J., Watt F. (2006) *Fabrication of buried channel waveguides in photosensitive glass using proton beam writing*, Applied Physics Letters, vol. 88, no 17.

[Bhardwaj *et al.*, 2005] Bhardwaj V., Simova E., Corkum P., Rayner D., Hnatovsky C., Taylor R., Schreder B., Kluge M., Zimmer J. (2005) *Femtosecond laser-induced refractive index modification in multicomponent glasses*, Journal of Applied Physics, vol. 97, no 8.

[Cheng *et al.*, 2005] Cheng Y., Sugioka K., Midorikawa K. (2005) *Freestanding optical fibers fabricated in a glass chip using femtosecond laser micromachining for lab-on-a-chip application*, Optics Express, vol. 13, no 17.

[Cheng *et al.*, 2006] Cheng Y., Tsai H., Sugioka K., Midorikawa K. (2006) *Fabrication of 3D microoptical lenses in photosensitive glass using femtosecond laser micromachining*, Applied Physics A: Materials Science and Processing, vol. 85, no 1, p. 11–14.

[Cheng, Y. *et al.*, 2003] Cheng, Y., Sugioka, K., Masuda, M., Shihoyama, K., Toyoda, K., Midorikawa, K. (2003) *Optical gratings embedded in photosensitive glass by photochemical reaction using a femtosecond laser*, Optics Express, vol. 11, no 15, p. 1809–1816.

[Cheng, Y. *et al.*, 2005] Cheng, Y., Sugioka, K., Midorikawa, K. (2005) *Microfabrication of 3d hollow structures embedded in glass by femtosecond laser for Lab-on-a-chip applications*, Applied surface science, vol. 248, no 1-4, p. 172–176.

[Dario, P. *et al.*, 2000] Dario, P., Chiara Carrozza, M., Benvenuto, A., Menciassi A. (2000) *Micro-systems in biomedical applications*, Journal of Micromechanics and Microengineering, vol. 10, no 2, p. 235–244.

[Desbiens, 2006] Desbiens J.P. (2006) *Micro-Usinage au Laser excimère et prototypage de MEMS*, Master's thesis, Université de Sherbrooke.

[Dietrich, T.R. *et al.*, 1996] Dietrich, T.R., Ehrfeld, W., Lacher, M., Krämer, M., Speit, B. (1996) *Fabrication technologies for microsystems utilizing photoetchable glass*, Microelectronic Engineering, vol. 30, no 1-4, p. 497–504.

[Dubowski, 2005] Dubowski J.J. (2005) *Principes de base sur les lasers et microfabrication assistée par laser*, p. 5.29.

[Feng and Farris, 2002] Feng R., Farris R. (2002) *The characterization of thermal and elastic constants for an epoxy photoresist SU8 coating*, Journal of Materials Science, vol. 37, no 22, p. 4793–4799.

[Fisette *et al.*, 2006] Fisette B., Busque F., Degorce J.Y., Meunier M. (2006) *Three-dimensional crystallization inside photosensitive glasses by focused femtosecond laser*, Applied Physics Letters, vol. 88, no 9.

[Fisette and Meunier, 2004] Fisette B., Meunier M. (2004) *Femtosecond laser three-dimensional microstructuring inside photosensitive glasses*, Proceedings of SPIE - The International Society for Optical Engineering, vol. 5578, no PART 2, p. 677–686.

[Frechette *et al.*, 2000] Frechette L., Jacobson S., Breuer K., Ehrich F., Ghodssi R., Khanna R., Wong C.W., Zhang X., Schmidt M., Epstein A. (2000) *Demonstration of a microfabricated high-speed turbine supported on gas bearings*, Hilton Head Island, SC, USA, p. 43–7.

[Fruman, D.H., 2001] Fruman, D.H. (2001) *Small is beautiful, microhydrodynamics of yesterday, today and tomorrow.*

[Fuqua, P.D. *et al.*, 2000] Fuqua, P.D., Taylor, D.P., Helvajian, H., Hansen, W.W., Abraham, M.H. (2000) *A UV direct-write approach for formation of embedded structures in photostructurable glass-ceramics*, Materials Research Society Symposium - Proceedings, vol. 624, p. 79–86.

[Gomez-Morilla, I. *et al.*, 2005] Gomez-Morilla, I., Abraham, M.H., Kerckhove, D.G., Grime, G.W. (2005) *Micropatterning of Foturan photosensitive glass following exposure to MeV proton beams*, Journal of Micromechanics and Microengineering, vol. 15, no 4, p. 706–709.

[Ho, S. and Herman, R., 2004] Ho, S., Herman, R. (2004) *Direct ultrafast laser writing of buried waveguides in Foturan glass*, Conference on Lasers and Electroptics (CLEO), vol. 2, p. 3.

[Hongo *et al.*, 2005] Hongo T., Sugioka K., Niino H., Cheng Y., Masuda M., Miyamoto I., Takai H., Midorikawa K. (2005) *Investigation of photoreaction mechanism of photosensitive glass by femtosecond laser*, Journal of Applied Physics, vol. 97, no 6, multiphoton absorption;Femtosecond lasers;Photoreaction;Oxygen deficient center (ODC);.

[Janson *et al.*, 2005] Janson S., Huang A., Hansen W., Steffeney L., Helvajian H. (2005) *Development of an inspector satellite using photostructurable glass/ceramic materials*, Collection of Technical Papers - AIAA Space 2005 Conference and Exposition, vol. 3, p. 1529–1540.

[Janson, S.W. and Helvajian, H., 1999] Janson, S.W., Helvajian, H. (1999) *MEMS, Microengineering and Aerospace Systems*.

[Juodkazis, S. *et al.*, 2004] Juodkazis, S., Yamasaki, K., Mizeikis, V., Matsuo, S., Misawa, H. (2004) *Formation of embedded paterns in glasses using femtosecond irradiation*, Applied Physics A (Materials Science Processing), vol. A79, no 4-6, p. 1549–53.

[Karnakis, D.M. *et al.*, 2005] Karnakis, D.M., Knowles, M.R.H., Alty, K.T., Schlaf, M., Snelling, H.V. (2005) *Comparaison of glass processing using high repetition femtosecond (800nm) and UV (255nm) nanosecond pulsed lasers*, Progress in Biomedical Optics and Imaging - Proceedings of SPIE, vol. 5718, p. 216–227.

[Khan Malek *et al.*, 2006] Khan Malek C., Robert L., Boy J.J., Blind P. (2006) *Deep microstructuring in glass for microfluidic applications*, Microsystem Technologies, published online.

[Kim *et al.*, 2004] Kim J., Berberoglu H., Xu X. (2004) *Fabrication of microstructures in photoetchable glass ceramics using excimer and femtosecond lasers*, Journal of Microlithography, Microfabrication, and Microsystems, vol. 3, no 3, p. 478–485.

[Kim *et al.*, 2005] Kim J.E., Cho J.H., Paek S.H. (2005) *Functional membrane-implanted lab-on-a-chip for analysis of percent HDL cholesterol*, Analytical Chemistry, vol. 77, no 24, p. 7901–7907.

[Kösters, M. *et al.*, 2005] Kösters, M., Hsieh, H.T., Psaltis, D., Buse, K. (2005) *Holography in commercially available photoetchable glasses*, Applied Optics, vol. 44, no 17, p. 3399–402.

[Larangot, B. *et al.*,] Larangot, B., Rossi, C., Camps, T., Berthold, A. (????) *Solid propellant micro-rockets-towards a new type of power mems.*

[Livingston, F.E. *et al.*, 2004] Livingston, F.E., Adams, P.M., Helvajian, H. (2004) *Active Photo-Physical Processes in the Pulsed UV Nanosecond Laser Exposure of Photostructurable Glass Ceramic Materials*, Proceedings of SPIE - The International Society for Optical Engineering, vol. 5662, p. 44–50.

[Livingston, F.E. and Helvajian, H., 2005] Livingston, F.E., Helvajian, H. (2005) *Variable UV laser exposure processing of photosensitive glass-ceramics: Maskless micro- to meso-scale structure fabrication*, Applied Physics A: Materials Science and Processing, vol. 81, no 8, p. 1569–1581.

[Masuda, M. *et al.*, 2003] Masuda, M., Sugioka, K., Cheng, Y., Aoki, N., Kawachi, M., Shihoyama, K., Toyoda, K., Helvajian, H., Midorikawa, K. (2003) *3-D microstructuring inside photosensitive glass by femtosecond laser excitation*, Applied Physics A: Materials Science and Processing, vol. 76, no 5, p. 857–860.

[Rajta, I. *et al.*, 2003] Rajta, I., Gomez-Morilla, I., Abraham, M.H., Kiss, A.Z. (2003) *Proton beam micromachining on PMMA, Foturan and CR-39 materials*, Nuclear Instruments and Methods in Physics Research, Section B: Beam Interactions with Materials and Atoms, vol. 210, p. 260–265.

[Shaffer, E, 2007] Shaffer, E (2007) Master's thesis, Université de Sherbrooke.

[Sibailly and Richerzhagen, 2004] Sibailly O., Richerzhagen B. (2004) *Laser dicing of silicon and composite semiconductor materials*, Proceedings of SPIE - The International Society for Optical Engineering, vol. 5339, p. 394–397, explication de la méthode combinant laser et jet d'eau.

[Stillman *et al.*, 2007] Stillman J., Judy J., Helvajian H. (2007) *Processing parameters for the development of glass/ceramic MEMS*, vol. 6462, San Jose, CA, United States.

[Sugioka, K. *et al.*, 2005] Sugioka, K., Cheng, Y., Midorikawa, K. (2005) *Three-dimensional micromachining of glass using femtosecond laser for lab-on-a-chip device manufacture*, Applied Physics A: Materials Science and Processing, vol. 81, no 1, p. 1–10.

[Talkenberg *et al.*, 2002] Talkenberg M., Kreutz E.W., Horn A., Jacquorie M., Poprawe R. (2002) *UV laser radiation-induced modifications and microstructuring of glass*, Proceedings of SPIE - The International Society for Optical Engineering, vol. 4637, p. 258–269.

[Wikipedia, 2008] Wikipedia (2008) *Wikipédia, L'encyclopédie libre.*

[Wisniowski, 1999] Wisniowski H. (1999) *Analog Devices Puts Micromachines In Motion.*